A wave propagation method for compressible multiphase flow on mapped grids

K.-M. Shyue

Department of Mathematics, National Taiwan University, Taipei 106, Taiwan

Abstract

A simple interface-capturing approach to compressible homogeneous multiphase flow problems is developed for the Euler equations of gas dynamics with a stiffened gas equation of state on body-fitted mapped grids in general two- and three-dimensional geometries. The algorithm uses a generalized coordinate formulation of the equations that is derived to ensure the correct fluid mixing when approximating the equations numerically with material interfaces. A γ-based and a α-based model have been described that is an easy extension of the Cartesian coordinates counterpart devised previously by the author (K.-M. Shyue, An efficient shock-capturing algorithm for compressible multicomponent problems, J. Comput. Phys. 142 (1998) 208-242). A standard high-resolution wave propagation method is employed to solve the proposed multiphase models with the dimensional-splitting technique incorporated for an efficient implementation of the method to multidimensional problems. Several calculations are presented with an HLLC approximate Riemann solver that show accurate results obtained using the method without introducing any spurious oscillations in the pressure near the interfaces. This includes some validation tests for problems in two dimensions where our quadrilateral-grid results are in direct comparison with the ones obtained using a Cartesian grid embedded boundary method. Sample results for three-dimensional problems on hexahedral grids are shown also.

Key words: Compressible multiphase flow, Fluid mixture model, Body-fitted mapped grids, Wave propagation method, Stiffened gas equation of state

2000 MSC: 65M06, 65M50, 65Y15, 35L60, 58J45

Email address: shyue@math.ntu.edu.tw (K.-M. Shyue)

1. Introduction

Our goal is to describe a simple mapped-grid approach for efficient numerical resolution of compressible multiphase flows in two and three dimensions with complex geometries. As a first endeavor towards the method development, we are concerned with a simplified model problem, where the flow regime of interest is assumed to be homogeneous with no jumps in the pressure and velocity (the normal component of it) across the material interface separating two regions of different fluid components within a spatial domain. In this problem, the physical effects such as the viscosity, surface tension, and heat conduction are assumed to be small, and hence can be ignored. With that, we use an Eulerian viewpoint of the governing equations that the principal motion of each fluid component in a Cartesian coordinates can be written as

$$\frac{\partial}{\partial t}\begin{pmatrix}\rho \\ \rho u_i \\ E\end{pmatrix} + \sum_{j=1}^{N_d} \frac{\partial}{\partial x_j}\begin{pmatrix}\rho u_j \\ \rho u_i u_j + p\delta_{ij} \\ E u_j + p u_j\end{pmatrix} = 0 \tag{1}$$

for $i = 1, 2, \ldots, N_d$. Here N_d denotes the number of spatial dimensions. The quantities ρ, u_j, p, E, and δ_{ij} are the density, particle velocity in the x_j-direction, pressure, total energy, and the Kronecker delta, respectively.

To close the model, for simplicity, the constitutive law for each fluid phase is assumed to satisfy a linearized Mie-Grüneisen (*i.e.*, the linearly density-dependent stiffened gas) equation of state of the form

$$p(\rho, e) = (\gamma - 1)\,\rho e + (\rho - \rho_0)\,\mathcal{B} \tag{2}$$

for approximating materials including compressible liquids and solids (cf. [16, 29]). Here e represents the specific internal energy. The quantities γ, ρ_0, and $\mathcal{B}$ are the ratio of specific heats ($\gamma > 1$), the reference values of density, and speed of sound squared, respectively. We have $E = \rho e + \sum_{j=1}^{N_d} \rho u_j^2/2$ as usual.

In this work, we want to generalize a state-of-the-art shock-capturing method that was devised originally for single-phase flows on mapped grids to the case of a multiphase flow. It is well known that the principal problem in the usual extension is the occurrence of spurious pressure oscillations when two or more fluid components are present in a grid cell (cf. [5] and references therein). Here the algorithm uses a generalized coordinate formulation of a fluid-mixture model that is composed of the Euler equations of gas dynamics for the basic conserved variables and an additional set of effective equations for the problem-dependent material quantities. In this approach, as in its Cartesian coordinates counterpart (cf. [34, 35]), the latter equations are derived to ensure the correct fluid mixing when approximating the equations numerically with material interfaces, see Section 2. With the proposed model equations, accurate results can be obtained on a mapped grid using a standard method, such as the dimensional-splitting version of the high-resolution wave propagation method for a single-phase flow (cf. [10, 11, 26]), see Section 4 for numerical examples.

There are quite a few other numerical approaches available in the literature for approximating compressible multiphase problems over a multidimensional domain with complex geometries. Some representative ones are the unstructured meshes methods [2, 49], the overlapping grids method [5], and the Cartesian grid embedded boundary method [39].

An advantage of the mapped-grid approach described here is that extension of the method from two to three dimensions can be done in a straightforward manner for simple geometries such as cylinders, spheres, and their variants [11]. This is in contrast with the extension of an unstructured or a Cartesian grid method, where it requires a significant algorithmic and programming effort to realize each of the methods that are designed of general purpose. In addition to that, if we want to use a front tracking method to improve numerical resolution of shock waves and interfaces, with complex geometries involved, it would be relatively easier to apply the method on a body-fitted mapped grid than on a fixed Cartesian grid, see [22, 40] for an example.

It should be mentioned that the methodology we have given here is by no means limited to the current case with the stiffened gas equation of state. Extension of the method to problems involving more complicated equations of state can be made by considering, for instance, either a γ-based model of the author [36] or a α-based model of Allaire *et al.* [3] (see Section 2.2), and proceeding with the idea described in this paper. Without going into the details for that, our goal is to establish the basic solution strategy and validate its use via some sample numerical experimentations; this is a necessary step for our further development of the method towards more complicated problems of fundamental importance (cf. [19, 31, 32] and references therein).

The format of this paper is as follows. In Section 2, we describe our mathematical model for a simplified homogeneous multiphase flow in generalized coordinates. In Section 3, we review briefly the dimensional-splitting version of the wave propagation method, and give a discussion of the HLLC approximate Riemann solver for the solution of the normal Riemann problem at the cell edge. Numerical results of some sample test problems in two and three dimensions are presented in Section 4.

2. Mathematical models in generalized coordinate

The basic governing equations in our multiphase model consist of two parts. We use the Euler equations in a generalized coordinates as a model system for the motion of the fluid mixtures of the conserved variables in a multiphase grid cell. With that, from the mass and energy conservations, we derive a set of effective equations for the problem-dependent material quantities in those cells, see below, that can be used easily to the determination of the pressure from the equation of state. Combining this two set of the equations together with the equation of state constitutes a complete mathematical model that is fundamental in our mapped grid algorithm for numerical approximation of multiphase flow problems with complex geometries.

To find out the aforementioned equations in a three-dimensional $N_d = 3$ generalized coordinates, for example, we introduce a coordinate mapping from the physical domain (x_1, x_2, x_3) to the computational domain (ξ_1, ξ_2, ξ_3) via the relations

$$\begin{aligned} dx_1 &= a_1 d\xi_1 + a_2 d\xi_2 + a_3 d\xi_3, \\ dx_2 &= b_1 d\xi_1 + b_2 d\xi_2 + b_3 d\xi_3, \\ dx_3 &= c_1 d\xi_1 + c_2 d\xi_2 + c_3 d\xi_3, \end{aligned} \tag{3}$$

where a_i, b_i, c_i for $i = 1, 2, 3$ are the metric terms of the mapping. Then under the mapping (3), the Euler Eqs. (1) can be transformed into the new coordinate system as

$$\begin{aligned} &\frac{\partial \rho}{\partial t} + \frac{1}{J} \sum_{j=1}^{N_d} \frac{\partial}{\partial \xi_j} (\rho U_j) = 0, \\ &\frac{\partial}{\partial t} (\rho u_i) + \frac{1}{J} \sum_{j=1}^{N_d} \frac{\partial}{\partial \xi_j} (\rho u_i U_j + p J_{ji}) = 0, \quad i = 1, 2, \ldots, N_d, \\ &\frac{\partial E}{\partial t} + \frac{1}{J} \sum_{j=1}^{N_d} \frac{\partial}{\partial \xi_j} (E U_j + p U_j) = 0, \end{aligned} \tag{4}$$

where $U_j = \sum_{i=1}^{N_d} u_i J_{ji}$ is the contravariant velocity in the ξ_j-direction for $j = 1, 2, \ldots, N_d$. Here the quantities J_{ij} for $i, j = 1, 2, 3$ are as a consequence of the coordinates transformation that satisfies the following expressions:

$$\begin{bmatrix} J_{11} & J_{12} & J_{13} \\ J_{21} & J_{22} & J_{23} \\ J_{31} & J_{32} & J_{33} \end{bmatrix} = \begin{bmatrix} b_2c_3 - b_3c_2 & a_3c_2 - a_2c_3 & a_2b_3 - a_3b_2 \\ b_3c_1 - b_1c_3 & a_1c_3 - a_3c_1 & a_3b_1 - a_1b_3 \\ b_1c_2 - b_2c_1 & a_2c_1 - a_1c_2 & a_1b_2 - a_2b_1 \end{bmatrix}, \tag{5}$$

and $J = \det |\partial(x_1, x_2, x_3)/\partial(\xi_1, \xi_2, \xi_3)|$ is the Jacobian of the mapping which can be computed by

$$J = \sum_{i=1}^{3} a_i J_{1i} = \sum_{i=1}^{3} b_i J_{2i} = \sum_{i=1}^{3} c_i J_{3i}. \tag{6}$$

Note that during the initialization step for computations, all the coordinate transformation quantities such as a_i, b_i, c_i, J_{1i}, J_{2i}, J_{3i} for $i = 1, 2, 3$, and J would be determined and remained fixed at all time when a body-fitted grid is constructed by a chosen numerical grid generator (cf. [11, 44]).

It is easy to see that (3) would be a two-dimensional coordinate mapping from (x_1, x_2) to (ξ_1, ξ_2) for any spatial location x_3 in the physical domain, if we have a simplified data set where the quantities a_3, b_3, c_1, and c_2 are all zero, and c_3 is equal to one. In this instance, if we set $N_d = 2$ in (4) with the coordinate transformation variables defined as in (5) and (6), we would have the same Euler equations in a two-dimensional generalized coordinates when a mapping of the form

$$\begin{aligned} dx_1 &= a_1 d\xi_1 + a_2 d\xi_2, \\ dx_2 &= b_1 d\xi_1 + b_2 d\xi_2, \end{aligned}$$

is used in the derivation (cf. [4, 9, 20, 47]). Thus, without causing any confusion, we may simply use the symbol N_d as in the Cartesian case, see (1), to represent the number of spatial dimension in the generalized-coordinate formulation of equations.

2.1. γ-based model equations

To derive the effective equations for the mixture of material quantities in a stiffened gas equation of state (2), by following the same approach as discussed in [34, 36, 37, 38], we start with an interface-only problem as usual where both the pressure and each phase of the particle velocities are constant in the domain, while the other variables such as the density and the material quantities are having jumps across some interfaces. Then, from (4), it is easy to obtain an equation for the time-dependent behavior of the total internal energy as

$$\frac{\partial}{\partial t}(\rho e) + \frac{1}{J}\sum_{j=1}^{N_d} U_j \frac{\partial}{\partial \xi_j}(\rho e) = 0.$$

Now, by inserting (2) into the above equation, we find an alternative form:

$$\frac{\partial}{\partial t}\left(\frac{p}{\gamma-1} - \frac{\rho-\rho_0}{\gamma-1}\mathcal{B}\right) + \frac{1}{J}\sum_{j=1}^{N_d} U_j \frac{\partial}{\partial \xi_j}\left(\frac{p}{\gamma-1} - \frac{\rho-\rho_0}{\gamma-1}\mathcal{B}\right) = 0, \tag{7}$$

that is in relation to not only the pressure, but also the density and the material quantities γ, ρ_0, $\mathcal{B}$.

In our algorithm, to maintain the pressure in equilibrium as it should be for this interface-only problem and also to determine all the three material quantities in (2), we split (7) into the following three equations for the fluid mixture of $1/(\gamma-1)$, $\rho\mathcal{B}/(\gamma-1)$, and $\rho_0\mathcal{B}/(\gamma-1)$ as

$$\frac{\partial}{\partial t}\left(\frac{1}{\gamma-1}\right) + \frac{1}{J}\sum_{j=1}^{N_d} U_j \frac{\partial}{\partial \xi_j}\left(\frac{1}{\gamma-1}\right) = 0, \tag{8}$$

$$\frac{\partial}{\partial t}\left(\frac{\rho\mathcal{B}}{\gamma-1}\right) + \frac{1}{J}\sum_{j=1}^{N_d} U_j \frac{\partial}{\partial \xi_j}\left(\frac{\rho\mathcal{B}}{\gamma-1}\right) = 0, \tag{9}$$

$$\frac{\partial}{\partial t}\left(\frac{\rho_0\mathcal{B}}{\gamma-1}\right) + \frac{1}{J}\sum_{j=1}^{N_d} U_j \frac{\partial}{\partial \xi_j}\left(\frac{\rho_0\mathcal{B}}{\gamma-1}\right) = 0, \tag{10}$$

respectively. As before (cf. [35, 36, 37, 38]), since in practice we are interested in shock wave problems as well, we should take the equations, *i.e.*, (8), (9), and (10), in a form so that all the three material quantities remain unchanged across both shocks and rarefaction waves. In this regard, it is easy to see that with $1/(\gamma-1)$ and $\rho_0\mathcal{B}/(\gamma-1)$ governed in turn by (8) and (10), there is no problem to do so (cf. [1, 34]). For $\rho\mathcal{B}/(\gamma-1)$, however, due to the dependence of the density term, it turns out that, in a time when such a situation occurs, for consistent with the mass conservation law of the fluid mixture in (4), the primitive form of (9) should be modified by

$$\frac{\partial}{\partial t}\left(\frac{\rho\mathcal{B}}{\gamma-1}\right)+\frac{1}{J}\sum_{j=1}^{N_d}\frac{\partial}{\partial\xi_j}\left(\frac{\rho\mathcal{B}}{\gamma-1}U_j\right)=0, \tag{11}$$

so that the mass-conserving property of the solution in the single phase region can be acquired also.

In summary, combining the Euler equations (4) and the set of effective equations: (8), (10), and (11), yields a so-called γ-based model system as

$$\begin{aligned}
&\frac{\partial\rho}{\partial t}+\frac{1}{J}\sum_{j=1}^{N_d}\frac{\partial}{\partial\xi_j}\left(\rho U_j\right)=0,\\
&\frac{\partial}{\partial t}\left(\rho u_i\right)+\frac{1}{J}\sum_{j=1}^{N_d}\frac{\partial}{\partial\xi_j}\left(\rho u_i U_j+pJ_{ji}\right)=0, \quad i=1,2,\ldots,N_d,\\
&\frac{\partial E}{\partial t}+\frac{1}{J}\sum_{j=1}^{N_d}\frac{\partial}{\partial\xi_j}\left(EU_j+pU_j\right)=0,\\
&\frac{\partial}{\partial t}\left(\frac{1}{\gamma-1}\right)+\frac{1}{J}\sum_{j=1}^{N_d}U_j\frac{\partial}{\partial\xi_j}\left(\frac{1}{\gamma-1}\right)=0,\\
&\frac{\partial}{\partial t}\left(\frac{\rho_0\mathcal{B}}{\gamma-1}\right)+\frac{1}{J}\sum_{j=1}^{N_d}U_j\frac{\partial}{\partial\xi_j}\left(\frac{\rho_0\mathcal{B}}{\gamma-1}\right)=0,\\
&\frac{\partial}{\partial t}\left(\frac{\rho\mathcal{B}}{\gamma-1}\right)+\frac{1}{J}\sum_{j=1}^{N_d}\frac{\partial}{\partial\xi_j}\left(\frac{\rho\mathcal{B}}{\gamma-1}U_j\right)=0;
\end{aligned} \tag{12}$$

this gives us N_d+5 equations to be solved in total that is nicely independent of the number of fluid phases involved in the problem. With a system expressed in this way, there is no problem to compute all the state variables of interests, including the pressure from the equation of state

$$p=\left[E-\frac{\sum_{i=1}^{N_d}(\rho u_i)^2}{2\rho}+\left(\frac{\rho\mathcal{B}}{\gamma-1}\right)-\left(\frac{\rho_0\mathcal{B}}{\gamma-1}\right)\right]\Big/\left(\frac{1}{\gamma-1}\right). \tag{13}$$

For the ease of the latter discussion, it is useful to write (12) into a more compact expression by

$$\frac{\partial q}{\partial t} + \frac{1}{J}\sum_{j=1}^{N_d}\left(\frac{\partial}{\partial \xi_j} f_j(q) + B_j(q)\frac{\partial q}{\partial \xi_j}\right) = 0, \tag{14}$$

with

$$\begin{aligned}
q &= \left[\rho, \rho u_1, \ldots, \rho u_{N_d}, E, \frac{1}{\gamma-1}, \frac{\rho_0 \mathcal{B}}{\gamma-1}, \frac{\rho\mathcal{B}}{\gamma-1}\right]^T, \\
f_j &= \Big[\rho U_j, \rho u_1 U_j + pJ_{j1}, \ldots, \rho u_{N_d} U_j + pJ_{j,N_d}, EU_j + pU_j, \\
&\qquad 0, 0, \frac{\rho\mathcal{B}}{\gamma-1}U_j\Big]^T, \\
B_j &= \operatorname{diag}\left[0, 0, \ldots, 0, 0, U_j, U_j, 0\right],
\end{aligned} \tag{15}$$

for $j = 1, 2, \ldots, N_d$. Note that in the Cartesian coordinates case where the coordinate mapping quantities a_1, b_2, c_3 are all equal to one, while the remaining ones are all zeros, (14) reduces to

$$\frac{\partial q}{\partial t} + \sum_{j=1}^{N_d}\left(\frac{\partial}{\partial x_j} \breve{f}_j(q) + \breve{B}_j(q)\frac{\partial q}{\partial x_j}\right) = 0, \tag{16}$$

with $\breve{f}_j$ and $\breve{B}_j$ defined in turn by

$$\begin{aligned}
\breve{f}_j &= \Big[\rho u_j, \rho u_1 u_j + p\delta_{1j}, \ldots, \rho u_{N_d} u_j + p\delta_{3j}, Eu_j + pu_j, \\
&\qquad 0, 0, \frac{\rho\mathcal{B}}{\gamma-1}u_j\Big]^T, \\
\breve{B}_j &= \operatorname{diag}\left[0, 0, \ldots, 0, 0, u_j, u_j, 0\right],
\end{aligned} \tag{17}$$

Then it is easy to check that f_j and B_j are related to $\breve{f}_j$ and $\breve{B}_j$ via

$$f_j = \sum_{i=1}^{N_d} \breve{f}_i J_{ji} \quad \text{and} \quad B_j = \sum_{i=1}^{N_d} \breve{B}_i J_{ji},$$

respectively.

With these notations, by assuming the proper smoothness of the solutions, the quasi-linear form of our model (14) can be written as

$$\frac{\partial q}{\partial t} + \frac{1}{J}\sum_{j=1}^{N_d}\left(A_j(q) + B_j(q)\right)\frac{\partial q}{\partial \xi_j} = 0, \tag{18}$$

where $A_j = \partial f_j/\partial q = \sum_{i=1}^{N_d} \breve{A}_i J_{ji}$ is the Jacobian matrix of f_j with $\breve{A}_i = \partial \breve{f}_i/\partial q$ for $i = 1, 2, \ldots, N_d$. If we assume further that the thermodynamic description of the materials of interest is limited by the stability requirement, it is a straightforward matter to show that any linear combination of the matrices $\breve{A}_i + \breve{B}_i$ for $i = 1, 2, \ldots, N_d$ is diagonalizable with real eigenvalues and a complete set of linearly independent right eigenvectors (cf. [37]). Hence, we conclude that our multiphase model is hyperbolic. Regarding discontinuous solutions of the system, such as shock waves or contact discontinuities, we find the usual form of the Rankine-Hugoniot jump conditions across the waves (cf. [14]).

2.2. *α-based model equations*

Before proceeding further, it should be mentioned that to define the initial fluid mixtures $1/(\gamma-1)$, $\rho\mathcal{B}/(\gamma-1)$, and $\rho_0\mathcal{B}/(\gamma-1)$ in a grid cell that contains $m_f \geq 1$ different fluid phases where each of them occupies a distinct region with a volume-fraction function $\alpha_i \in [0, 1]$ in relation to it for $i = 1, 2, \ldots, m_f$, $\sum_{i=1}^{m_f} \alpha_i = 1$, we use the equation of state (2) of the form

$$\rho e = \sum_{i=1}^{m_f} \alpha_i \rho_i e_i = \sum_{i=1}^{m_f} \alpha_i \left(\frac{p_i}{\gamma_i - 1} - \frac{\rho_i - \rho_{0,i}}{\gamma_i - 1}\mathcal{B}_i\right) = \frac{p}{\gamma - 1} - \frac{\rho - \rho_0}{\gamma - 1}\mathcal{B}.$$

Here the subscript "i" denotes the state variable of fluid phase i. By taking a similar approach as employed in Section 2.1 for the derivation of the γ-based effective equations it comes out readily a splitting of the above expression into the relations:

$$\frac{1}{\gamma - 1} = \sum_{i=1}^{m_f} \frac{\alpha_i}{\gamma_i - 1}, \quad \frac{\rho\mathcal{B}}{\gamma - 1} = \sum_{i=1}^{m_f} \frac{\alpha_i \rho_i \mathcal{B}_i}{\gamma_i - 1}, \quad \frac{\rho_0\mathcal{B}}{\gamma - 1} = \sum_{i=1}^{m_f} \frac{\alpha_i \rho_{0,i} \mathcal{B}_i}{\gamma_i - 1} \tag{19}$$

where in the process of splitting the terms the pressure p is chosen to fulfill the condition

$$\frac{p}{\gamma - 1} = \sum_{i=1}^{m_f} \frac{\alpha_i p_i}{\gamma_i - 1}. \tag{20}$$

Clearly when each of the partial pressures is in an equilibrium state within a grid cell, in conjunction with the first part of (19), the pressure p obtained from (20) would remain in the same equilibrium as well, *i.e.*, $p = p_i$ for $i = 1, 2, \ldots, m_f$.

Now if the above volume-fraction notion of the states $1/(\gamma - 1)$, $\rho\mathcal{B}/(\gamma - 1)$, and $\rho_0\mathcal{B}/(\gamma - 1)$ are being employed in the γ-based effective equations together with the usual definition of the mixture density $\rho = \sum_{i=1}^{m_f} \alpha_i\rho_i$, we are able to rewrite them straightforwardly into a componentwise form as

$$\frac{\partial}{\partial t}\left(\frac{\alpha_i}{\gamma_i - 1}\right) + \frac{1}{J}\sum_{j=1}^{N_d} U_j \frac{\partial}{\partial \xi_j}\left(\frac{\alpha_i}{\gamma_i - 1}\right) = 0, \tag{21}$$

$$\frac{\partial}{\partial t}\left(\frac{\alpha_i\rho_i\mathcal{B}_i}{\gamma_i - 1}\right) + \frac{1}{J}\sum_{j=1}^{N_d} \frac{\partial}{\partial \xi_j}\left(\frac{\alpha_i\rho_i\mathcal{B}_i}{\gamma_i - 1}U_j\right) = 0, \tag{22}$$

$$\frac{\partial}{\partial t}\left(\frac{\alpha_i\rho_{0,i}\mathcal{B}_i}{\gamma_i - 1}\right) + \frac{1}{J}\sum_{j=1}^{N_d} U_j \frac{\partial}{\partial \xi_j}\left(\frac{\alpha_i\rho_{0,i}\mathcal{B}_i}{\gamma_i - 1}\right) = 0, \tag{23}$$

$i = 1, 2, \ldots, m_f$. Then based on the fact that all the material quantities γ_i, $\mathcal{B}_i$, and $\rho_{0,i}$ will be kept as a constant in each phase of the domain at all time, from (21) or (23) , it is easy to find the transport equation for the volume fraction α_i as

$$\frac{\partial \alpha_i}{\partial t} + \frac{1}{J}\sum_{j=1}^{N_d} U_j \frac{\partial \alpha_i}{\partial \xi_j} = 0, \tag{24}$$

whereas, from (22), we find the conservation law for the phasic density $\alpha_i\rho_i$ as

$$\frac{\partial}{\partial t}(\alpha_i\rho_i) + \frac{1}{J}\sum_{j=1}^{N_d} \frac{\partial}{\partial \xi_j}(\alpha_i\rho_i U_j) = 0. \tag{25}$$

It is apparent that, if the solutions of α_i and $\alpha_i\rho_i$ are known from the equations for $i = 1, 2, \ldots, m_f$, we may, therefore, compute $1/(\gamma - 1)$, $\rho\mathcal{B}/(\gamma - 1)$, and $\rho_0\mathcal{B}/(\gamma - 1)$ directly according to (19). Thus, instead of using the γ-based effective equations, it is a viable alternate to use the α-based equations: (24) and (25), for the motion of the mixture of the material quantities of the problem.

To sum up, combining (24) and (25) with the momentum and energy equations in (4) yields a α-based (or called volume-fraction) model system that can be written as

$$
\begin{aligned}
&\frac{\partial}{\partial t}(\alpha_i\rho_i) + \frac{1}{J}\sum_{j=1}^{N_d}\frac{\partial}{\partial \xi_j}(\alpha_i\rho_i U_j) = 0, \quad i = 1, 2, \ldots, m_f \\
&\frac{\partial}{\partial t}(\rho u_i) + \frac{1}{J}\sum_{j=1}^{N_d}\frac{\partial}{\partial \xi_j}(\rho u_i U_j + pJ_{ji}) = 0, \quad i = 1, 2, \ldots, N_d, \\
&\frac{\partial E}{\partial t} + \frac{1}{J}\sum_{j=1}^{N_d}\frac{\partial}{\partial \xi_j}(EU_j + pU_j) = 0, \\
&\frac{\partial \alpha_i}{\partial t} + \frac{1}{J}\sum_{j=1}^{N_d} U_j\frac{\partial \alpha_i}{\partial \xi_j} = 0, \quad i = 1, 2, \ldots, m_f - 1;
\end{aligned}
\tag{26}
$$

this gives us totally $2m_f + N_d$ equations to be solved. Here analogously to (13) the pressure can be determined from the equation of state

$$
p = \left[E - \frac{\sum_{i=1}^{N_d}(\rho u_i)^2}{2\rho} + \sum_{i=1}^{m_f}\frac{\alpha_i\rho_i\mathcal{B}_i}{\gamma_i - 1} - \sum_{i=1}^{m_f}\frac{\alpha_i\rho_{0,i}\mathcal{B}_i}{\gamma_i - 1}\right] \Big/ \sum_{i=1}^{m_f}\frac{\alpha_i}{\gamma_i - 1}, \tag{27}
$$

where we have assumed $\alpha_{m_f} = 1 - \sum_{i=1}^{m_f - 1}\alpha_i$.

It is clear that (26) can be written of the form (14) in which we have q, f_j, and B_j defined by

$$
\begin{aligned}
q &= \left[\alpha_1\rho_1, \ldots, \alpha_{m_f}\rho_{m_f}, \rho u_1, \ldots, \rho u_{N_d}, E, \alpha_1, \ldots, \alpha_{m_f - 1}\right]^T, \\
f_j &= \left[\alpha_1\rho_1 U_j, \ldots, \alpha_{m_f}\rho_{m_f} U_j, \rho u_1 U_j + pJ_{j1}, \ldots, \rho u_{N_d} U_j + pJ_{j,N_d},\right. \\
&\qquad \left. EU_j + pU_j, 0, \ldots, 0\right]^T, \\
B_j &= \operatorname{diag}\left[0, \ldots, 0, \ldots, 0, U_j, \ldots, U_j\right].
\end{aligned}
\tag{28}
$$

In a similar manner, in the Cartesian coordinates case where the system is of the form (16), we have $\breve{f}_j$ and $\breve{B}_j$ defined by

$$
\begin{aligned}
\breve{f}_j &= \left[\alpha_1\rho_1 u_j, \ldots, \alpha_{m_f}\rho_{m_f} u_j, \rho u_1 u_j + p\delta_{j1}, \ldots, \rho u_{N_d} u_j + p\delta_{j,N_d},\right. \\
&\qquad \left. Eu_j + pu_j, 0, \ldots, 0\right]^T, \\
\breve{B}_j &= \operatorname{diag}\left[0, \ldots, 0, \ldots, 0, u_j, \ldots, u_j\right].
\end{aligned}
\tag{29}
$$

We note that since the derivation of the α-based model follows closely to the γ-based model, it can be shown that this model is hyperbolic also (cf. [3]

for the Cartesian coordinate case) and is as effective as the γ-based model for multiphase flow problems with the stiffened gas equation of state. But for problems with $m_f \geq 3$, the γ-based model is a prefer one to use, because the basic equations for the model stay as $N_d + 5$, see (12), irrespective of the number of fluid phases involved in the problem.

2.3. Include source terms

To end this section, we comment that if x_1 is the axisymmetric direction, an axisymmetric version of our multiphase models in two dimensions can be written as

$$\frac{\partial q}{\partial t} + \frac{1}{J} \sum_{j=1}^{2} \left(\frac{\partial}{\partial \xi_j} f_j(q) + B_j(q) \frac{\partial q}{\partial \xi_j} \right) = \psi(q), \tag{30}$$

where ψ is the source term derived directly from the geometric simplification. We find

$$\psi = -\frac{1}{x_1} \left[\rho u_1, \rho u_1^2, \rho u_1 u_2, (E + p) u_1, 0, 0, \frac{\rho \mathcal{B}}{\gamma - 1} u_1 \right]^T, \tag{31}$$

when the γ-based model is considered, and have

$$\psi = -\frac{1}{x_1} \left[\alpha_1 \rho_1 u_1, \ldots, \alpha_{m_f} \rho_{m_f} u_{m_f}, \rho u_1^2, \rho u_1 u_2, (E + p) u_1, 0, \ldots, 0 \right]^T, \tag{32}$$

when the α-based model is considered. In addition to that, if gravity is the only body force in the problem formulation, in the γ-based model, for example, we may add in the following source term:

$$\psi = -\left[0,\ 0,\ \rho g,\ \rho g u_2,\ 0,\ 0,\ 0\right]^T \tag{33}$$

as well. Here g denotes the gravitational constant, and is set to be $9.81 \mathrm{m/s}^2$ in the computations done in Section 4.1.7. As to the other source terms such as the one arise from the surface tension force at the interface, we may use a continuum surface force model of Brackbill *et al.* [7] for that, see the work done by Perigaud and Saurel [30] and the references therein for more details. Since it is beyond the scope of this paper, we will not discuss this further.

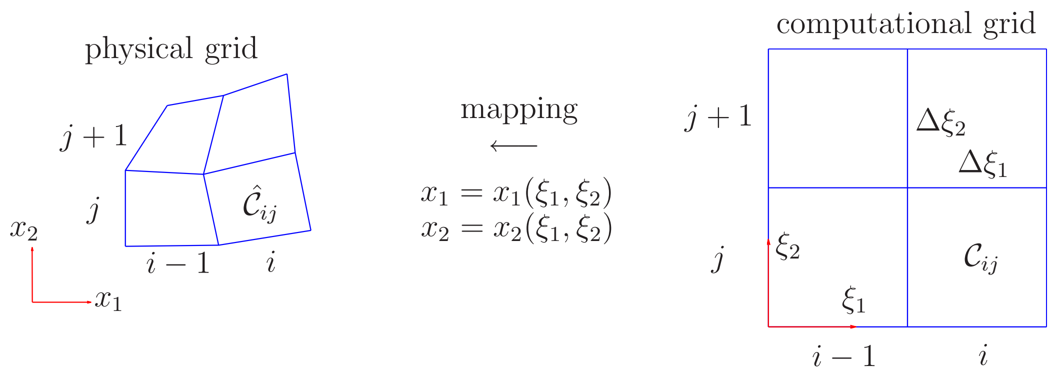

Figure 1: A sample grid system in our two-dimensional numerical method on a quadrilateral grid. The numerical solution on the rectangular grid cell $\mathcal{C}_{ij}$ in the computational domain gives distinctively the result on the mapped quadrilateral grid cell $\hat{\mathcal{C}}_{ij}$ in the physical domain for all the grid cell (i, j).

3. Numerical approximations

To find approximate solutions of our multiphase flow models on a mapped grid, we use a standard high-resolution wave propagation method developed by LeVeque [23, 25, 26] for general hyperbolic systems of partial differential equations. For simplicity, we consider the two-dimensional case $N_d = 2$ as an example, and will describe the method briefly on a uniform rectangular grid with a fixed mesh spacing $\Delta\xi_1$ in the ξ_1-direction and $\Delta\xi_2$ in the ξ_2-direction that discretizes a computational domain as illustrated in Fig. 1, for instance.

The method we employ is based on a finite-volume formulation in which the approximate value Q_{ij}^n of the cell average of the solution over the (i, j)th grid cell at a time t_n can be written as

$$Q_{ij}^n \approx \frac{1}{J_{ij}\Delta\xi_1\Delta\xi_2} \int_{\mathcal{C}_{ij}} q(\xi_1, \xi_2, t_n)\, d\xi_1\, d\xi_2,$$

where $\mathcal{C}_{ij}$ denotes the rectangular region occupied by the grid cell (i, j). Note that in the current setup the numerical solution on the rectangular grid cell $\mathcal{C}_{ij}$ in the computational domain gives distinctively the result on the mapped quadrilateral grid cell $\hat{\mathcal{C}}_{ij}$ in the physical domain for all the grid cell (i, j), see Fig. 1. The time step from the current time t_n to the next t_{n+1} is denoted by Δt.

3.1. First-order wave propagation method

In a simple dimensional-splitting approach, the equations to be solved, *i.e.*, (14), are split into a sequence of one-dimensional problems as

$$\xi_1\text{-sweeps:} \qquad \frac{\partial q}{\partial t} + \frac{1}{J}\frac{\partial f_1(q)}{\partial \xi_1} + B_1(q)\frac{1}{J}\frac{\partial q}{\partial \xi_1} = 0, \tag{34}$$

$$\xi_2\text{-sweeps:} \qquad \frac{\partial q}{\partial t} + \frac{1}{J}\frac{\partial f_2(q)}{\partial \xi_2} + B_2(q)\frac{1}{J}\frac{\partial q}{\partial \xi_2} = 0, \tag{35}$$

and so in each time step a dimensional-splitting (or called Godunov-splitting) version of the first-order wave propagation method in two dimensions can be written as

$$Q_{ij}^{*} = Q_{ij}^{n} - \frac{1}{J_{ij}}\frac{\Delta t}{\Delta \xi_1}\left[\left(\mathcal{A}_1^{+}\Delta Q\right)_{i-1/2,j}^{n} + \left(\mathcal{A}_1^{-}\Delta Q\right)_{i+1/2,j}^{n}\right], \tag{36}$$

$$Q_{ij}^{n+1} = Q_{ij}^{*} - \frac{1}{J_{ij}}\frac{\Delta t}{\Delta \xi_2}\left[\left(\mathcal{A}_2^{+}\Delta Q\right)_{i,j-1/2}^{*} + \left(\mathcal{A}_2^{-}\Delta Q\right)_{i,j+1/2}^{*}\right]. \tag{37}$$

Here in the ξ_1-sweeps we start with the cell average Q_{ij}^n at a time t_n and solve (34) along each row of cells $\mathcal{C}_{ij}$ with j fixed, updating Q_{ij}^n to Q_{ij}^* by the use of (36) with the fluctuations

$$(\mathcal{A}_1^{+}\Delta Q)_{i-1/2,j}^{n} = \sum_{m=1}^{m_w}\left(\lambda_{1,m}^{+}\mathcal{W}_{1,m}\right)_{i-1/2,j}^{n}$$

and

$$(\mathcal{A}_1^{-}\Delta Q)_{i+1/2,j}^{n} = \sum_{m=1}^{m_w}\left(\lambda_{1,m}^{-}\mathcal{W}_{1,m}\right)_{i+1/2,j}^{n},$$

where $(\lambda_{1,m})_{\iota-1/2,j}^n$ and $(\mathcal{W}_{1,m})_{\iota-1/2,j}^n$ are in turn the wave speed and the jump of the wave for the mth family of the solutions obtained from solving the one-dimensional Riemann problems in the direction normal to the cell interface between $\mathcal{C}_{\iota-1,j}$ and $\mathcal{C}_{\iota j}$ with a properly chosen solver, see Section 3.3, for $\iota = i, i+1$. As usual, the notations for $\lambda^{\pm}$ are set by $\lambda^{+} = \max(\lambda, 0)$ and $\lambda^{-} = \min(\lambda, 0)$.

Then in the ξ_2-sweeps we can use the Q_{ij}^* values as data for solving (35) along each column of cells $\mathcal{C}_{ij}$ with i fixed, which gives us the solution of the next time step Q_{ij}^{n+1} from (37) with the fluctuations

$$(\mathcal{A}_2^{+}\Delta Q)_{i,j-1/2}^{*} = \sum_{m=1}^{m_w}\left(\lambda_{2,m}^{+}\mathcal{W}_{2,m}\right)_{i,j-1/2}^{*}$$

and

$$(\mathcal{A}_2^- \Delta Q)^*_{i,j+1/2} = \sum_{m=1}^{m_w} \left(\lambda^-_{2,m} \mathcal{W}_{2,m} \right)^*_{i,j+1/2}.$$

Clearly this method belongs to a class of upwind schemes, and is stable when the typical CFL (Courant-Friedrichs-Lewy) condition:

$$\nu = \frac{\Delta t \max_m (\lambda_{1,m}, \lambda_{2,m})}{\min (\Delta\xi_1, \Delta\xi_2)} \le 1, \tag{38}$$

is satisfied (cf. [26]). Moreover, it is not difficult to show that the method is quasi-conservative in the sense that when applying the method to (14) not only the conservation laws but also the transport equations are approximated in a consistent manner by the method (cf. [34, 35, 37]).

3.2. High-resolution wave propagation method

To extend this splitting method to a high-resolution version (*i.e.*, second-order accurate on smooth solutions, and sharp and monotone profiles on discontinuous solutions), it is a common practice to use the Strang splitting [41] and introduce slopes and limiter to the method as in many other high-resolution schemes for hyperbolic conservation laws [24, 42]. Without going into the details for that, see [26] for more expositions on the current mapped grid case, in each time step, the first order method described in Section 3.1 is modified by the following steps:

$$\begin{aligned}
Q^*_{ij} &= Q^n_{ij} - \frac{1}{J_{ij}} \frac{\Delta t}{2\Delta\xi_1} \Bigg[\left(\mathcal{A}_1^+ \Delta Q\right)^n_{i-1/2,j} + \left(\mathcal{A}_1^- \Delta Q\right)^n_{i+1/2,j} + \\
&\qquad \left(\tilde{\mathcal{F}}_1\right)^n_{i+1/2,j} - \left(\tilde{\mathcal{F}}_1\right)^n_{i-1/2,j} \Bigg], \\
Q^{**}_{ij} &= Q^*_{ij} - \frac{1}{J_{ij}} \frac{\Delta t}{\Delta\xi_2} \Bigg[\left(\mathcal{A}_2^+ \Delta Q\right)^*_{i,j-1/2} + \left(\mathcal{A}_2^- \Delta Q\right)^*_{i,j+1/2} + \\
&\qquad \left(\tilde{\mathcal{F}}_2\right)^*_{i,j+1/2} - \left(\tilde{\mathcal{F}}_2\right)^*_{i,j-1/2} \Bigg], \\
Q^{n+1}_{ij} &= Q^{**}_{ij} - \frac{1}{J_{ij}} \frac{\Delta t}{2\Delta\xi_1} \Bigg[\left(\mathcal{A}_1^+ \Delta Q\right)^{**}_{i-1/2,j} + \left(\mathcal{A}_1^- \Delta Q\right)^{**}_{i+1/2,j} + \\
&\qquad \left(\tilde{\mathcal{F}}_1\right)^{**}_{i+1/2,j} - \left(\tilde{\mathcal{F}}_1\right)^{**}_{i-1/2,j} \Bigg].
\end{aligned}$$

Here in the above formulas the terms such as $(\tilde{\mathcal{F}}_1)^n_{i-1/2,j}$ and $(\tilde{\mathcal{F}}_2)^*_{i,j-1/2}$, for instance, are the high-resolution correction of the method which is defined by

$$(\tilde{\mathcal{F}}_1)^n_{i-1/2,j} = \frac{1}{2}\sum_{m=1}^{m_w}\left[|\lambda_{1,m}|\left(1-\frac{\Delta t}{2J_0\Delta\xi_1}|\lambda_{1,m}|\right)\tilde{\mathcal{W}}_{1,m}\right]^n_{i-1/2,j}$$

and

$$(\tilde{\mathcal{F}}_2)^*_{i,j-1/2} = \frac{1}{2}\sum_{m=1}^{m_w}\left[|\lambda_{2,m}|\left(1-\frac{\Delta t}{J_0\Delta\xi_2}|\lambda_{2,m}|\right)\tilde{\mathcal{W}}_{2,m}\right]^*_{i,j-1/2},$$

respectively. Note that J_0 is an averaged value of the grid Jacobian for grid cells to the left and right of the cell edge. The quantity $\tilde{\mathcal{W}}_{\iota,m}$ is a limited value of $\mathcal{W}_{\iota,m}$ obtained by comparing $\mathcal{W}_{\iota,m}$ with the corresponding $\mathcal{W}_{\iota,m}$ from the neighboring Riemann problem to the left (if $\lambda_{\iota,m} > 0$) or to the right (if $\lambda_{\iota,m} < 0$) for $\iota = 1, 2$.

3.3. Riemann problem and HLLC approximate solver

To determine the waves, speeds, and fluctuations in the aforementioned wave propagation methods, we need to solve the one-dimensional Riemann problems normal to each cell interface. If we consider the case at an edge between cells $\mathcal{C}_{i-1,j}$ and $\mathcal{C}_{ij}$ as illustrated in Fig. 1, for example, it amounts to solve a Cauchy problem in the direction $\vec{n}_{i-1/2,j}$ that consists of (34) as for the equations and the piecewise constant data

$$q(\xi_1, t_n) = \begin{cases} Q^n_{i-1,j} & \text{if} \quad \xi_1 < (\xi_1)_{i-1/2}, \\ Q^n_{ij} & \text{if} \quad \xi_1 > (\xi_1)_{i-1/2} \end{cases} \tag{39}$$

as for the initial condition at a time t_n. To do so, here we take a popular approach (cf. [5, 26]) in that the normal and tangential components of velocity are determined first from $Q^n_{i-1,j}$ and $Q^n_{i,j}$, relabeling these as the "x_1" and "x_2" components, and then the Riemann problem in the "x_1" direction is solved with this modified data. We, therefore, recombine the velocity components of the resulting Riemann problem solution to obtain the proper updates in the physical space. This is conceptually easier to implement in the current case because a Riemann solver has already been written for an analogous model system in Cartesian coordinates (cf. [35, 37, 38]). Note that in the applications concerned here we have chosen the data in (39) well enough so that the solution of the Riemann problem would consist of genuinely nonlinear waves such as shock and rarefaction, and linearly degenerate wave such as contact discontinuity; there is no vacuum region occurring in the solution.

Without loss of generality, we consider the γ-based model (12) as an example that the case for the α-based model (26) can be constructed in an analogously manner. In this case, with $\vec{n}_{i-1/2,j} = (\hat{b}_2, -\hat{a}_2)_{i-1/2,j}$ given a priori, our first step of the Riemann solver is to transform the data $Q^n_{i-1,j}$ and $Q^n_{i,j}$ into the new data $\breve{Q}_l$ and $\breve{Q}_r$ via

$$\breve{Q}_l = \mathcal{R}_{i-1/2,j} Q^n_{i-1,j}, \quad \breve{Q}_r = \mathcal{R}_{i-1/2,j} Q^n_{i,j},$$

where $\mathcal{R}_{i-1/2,j}$ is a rotation matrix defined by

$$\mathcal{R}_{i-1/2,j} = \begin{bmatrix} 1 & 0 & 0 & 0 \\ 0 & (\hat{b}_2)_{i-1/2,j} & -(\hat{a}_2)_{i-1/2,j} & 0 \\ 0 & (\hat{a}_2)_{i-1/2,j} & (\hat{b}_2)_{i-1/2,j} & 0 \\ 0 & 0 & 0 & I \end{bmatrix}$$

with I in it as being a 4×4 identity matrix. Clearly this rotation matrix rotates the velocity components of Q into components normal and tangential to the cell edge, and leaves the remaining components unchanged.

Having obtained the Riemann data $\breve{Q}_l$ and $\breve{Q}_r$, our next step is to solve

$$\frac{\partial q}{\partial t} + \frac{\partial}{\partial x_1} \breve{f}_1(q) + \breve{B}_1(q) \frac{\partial q}{\partial x_1} = 0 \tag{40}$$

in the "x_1" direction with $\breve{f}_1$ and $\breve{B}_1$ defined by (17). For that, among various methods proposed in the literature (cf. [45]), here we are interested in a simple and yet accurate variant of the approximate solver devised by Harten, Lax, and van Leer [17] for hyperbolic systems of conservation laws in that rather than introducing two discontinuities propagating at constant speeds λ_l and λ_r to the left and right, $\lambda_l \neq \lambda_r$, separating three constant states in the space-time domain, an additional middle wave of speed λ_m is included in the solution structure for modeling the speed of contact discontinuity, yielding a so-called 3-wave HLL (or called HLLC) solver (cf. [6, 45, 46] and references therein). Note that if we assume further that λ_l and λ_r are known a priori by some simple estimates based on the local information of the wave speeds, say, by taking

$$\lambda_l = \min\left(v_l - c_l,\ v_r - c_r\right),$$
$$\lambda_r = \max\left(v_l + c_l,\ v_r + c_r\right),$$

for instance, with $v_\iota = \breve{Q}_\iota^{(2)}/\breve{Q}_\iota^{(1)}$ and $c_\iota = (\sqrt{\gamma(p+p_0)/\rho})_\iota$ for $\iota = l$ or r, then it is easy to find the constant state in the middle region of the original 2-wave HLL solver as

$$\breve{Q}_m = \frac{\lambda_r \breve{Q}_r - \lambda_l \breve{Q}_l - \breve{f}_1(\breve{Q}_r) + \breve{f}_1(\breve{Q}_l)}{\lambda_r - \lambda_l}, \tag{41}$$

and set $\lambda_m = \breve{Q}_m^{(2)}/\breve{Q}_m^{(1)}$, where $\breve{Q}_m^{(i)}$ is the ith component of the vector $\breve{Q}_m$, see [45] for the other possible choices on the wave speeds.

With that, it is not difficult to find the constant states $\breve{Q}_{ml}$ and $\breve{Q}_{mr}$ in the regions m_l and m_r to the left and right of the middle wave, respectively, and the results are

$$\begin{aligned}\breve{Q}_{m\iota} = \Big[& h_{m\iota}^{(1)}, \lambda_m h_{m\iota}^{(1)}, \breve{Q}_\iota^{(3)} h_{m\iota}^{(1)}/\breve{Q}_\iota^{(1)}, h_{m\iota}^{(4)} + \lambda_m \left(\lambda_m h_{m\iota}^{(1)} - h_{m\iota}^{(2)}\right), \\ & \breve{Q}_\iota^{(5)}, \breve{Q}_\iota^{(6)}, h_{m\iota}^{(7)} \Big]^T,\end{aligned} \tag{42}$$

where we have set

$$h_{m\iota}^{(i)} = \frac{\lambda_\iota \breve{Q}_\iota^{(i)} - \breve{f}_1^{(i)}(\breve{Q}_\iota)}{\lambda_\iota - \lambda_m}$$

for $\iota = l$ or r. It should be mentioned that the states $\breve{Q}_{ml}^{(i)}$ and $\breve{Q}_{mr}^{(i)}$ satisfy the basic consistency condition of the integral form of the conservation laws,

$$\left(\frac{\lambda_m - \lambda_l}{\lambda_r - \lambda_l}\right) \breve{Q}_{ml}^{(i)} + \left(\frac{\lambda_r - \lambda_m}{\lambda_r - \lambda_l}\right) \breve{Q}_{mr}^{(i)} = \breve{Q}_m^{(i)}, \quad i = 1, 2, \ldots, 4, \text{and } 7.$$

The solution of this Riemann problem in the "x_1" direction is then composed of the three moving discontinuities:

$$\lambda_1 = \lambda_l, \quad \lambda_2 = \lambda_m, \quad \lambda_3 = \lambda_r$$

and the jumps across each of them by

$$\breve{\mathcal{W}}_1 = \breve{Q}_{ml} - \breve{Q}_l, \quad \breve{\mathcal{W}}_2 = \breve{Q}_{mr} - \breve{Q}_{ml}, \quad \breve{\mathcal{W}}_3 = \breve{Q}_r - \breve{Q}_{mr}.$$

To get the proper Riemann problem solution in the ξ_1 direction that was considered originally in the beginning of this subsection, we should set the speeds by

$$(\lambda_{1,m})_{i-1/2,j}^n = (S_2)_{i-1/2,j} \lambda_m, \quad m = 1, 2, 3,$$

where $(S_2)_{i-1/2,j} = (\sqrt{a_2^2 + b_2^2})_{i-1/2,j}$ is a scale factor, and the waves by

$$(\mathcal{W}_{1,m})^n_{i-1/2,j} = \mathcal{R}^{-1}_{i-1/2,j} \breve{\mathcal{W}}_m, \quad m = 1, 2, 3.$$

Here $\mathcal{R}^{-1}_{i-1/2,j}$ is the inverse of the rotation matrix given above. Having obtained the speeds and waves, we can then compute the fluctuations at the cell edge as

$$(\mathcal{A}_1^{\pm} \Delta Q)^n_{i-1/2,j} = \sum_{m=1}^{3} \left(\lambda^{\pm}_{1,m} \mathcal{W}_{1,m}\right)^n_{i-1/2,j},$$

and this would be used in the wave propagation method for the solution updates.

To end this section, we want to mention that the extension of this wave propagation method from two to three space dimensions can be done in a straightforward manner when the solutions of one-dimensional Riemann problems in each dimensional-sweep can be computed readily (cf. [21]). As to the implementation issue of the method on mapped grids in three dimensions, in particular, it is very useful to consult the public software package CLAWPACK at the web-site:

http://www.amath.washington.edu/~rjl/pubs/circles/index.html,

for that.

4. Numerical Results

We now present numerical results to validate our mapped grid algorithm described in Section 3 for compressible multiphase flow problems in two and three dimensions. Without stated otherwise, we have carried out all the tests using the Courant number $\nu = 0.9$ defined by (38), and the MINMOD limiter in the high-resolution version of the finite-volume wave propagation method. For comparison purposes, in some cases considered below, we have also included results obtained using a Cartesian grid embedded boundary method (cf. [23, 39]) to the problems.

We note that in this section we have only present solutions obtained using the γ-based model (12) to the method. This is because we have found a little difference between the results as compared to the ones using the α-based model (26) to the method for simulations. The computer programs (written in Fortran 77) used to obtain the results shown here are available from the author upon request.

4.1. Two-dimensional case

4.1.1. Smooth vortex flow

We begin our tests by performing a convergence study of the computed solutions for a two-dimensional vortex evolution problem (cf. [13, 33, 49]) that shows the order of accuracy that is attained for our high resolution method as the mesh is refined. In this problem, we assume a single-phase ideal gas flow with $\gamma = 1.4$ and $\mathcal{B} = 0$ in the stiffened gas equation of state (2). Initially, over a square domain of size $[0, 10] \times [0, 10]$, the state variables for the vortex are set by

$$
\begin{aligned}
\rho &= \left(1 - \frac{(\gamma-1)\epsilon^2}{8\gamma\pi^2} \exp\left(1 - r^2\right)\right)^{1/(\gamma-1)}, \\
p &= \rho^\gamma, \\
u_1 &= 1 - \frac{\epsilon}{2\pi} \exp\left(\left(1 - r^2\right)/2\right)\left(x_2 - \bar{x}_2\right), \\
u_2 &= 1 + \frac{\epsilon}{2\pi} \exp\left(\left(1 - r^2\right)/2\right)\left(x_1 - \bar{x}_1\right),
\end{aligned}
$$

where $r = \sqrt{(x_1 - \bar{x}_1)^2 + (x_2 - \bar{x}_2)^2}$ is the distance between points (x_1, x_2) and the vortex center $(\bar{x}_1, \bar{x}_2) = (5, 5)$, and $\epsilon = 5$ is the vortex strength. Note that the above states are as the results of an isentropic perturbation in p/ρ, u_1, and u_2 to the mean flow with $\bar{\rho} = 1$, $\bar{p} = 1$, $\bar{u}_1 = 1$, and $\bar{u}_2 = 1$, and it is known that with the periodic conditions in both the x_1- and x_2-direction the exact solution for this problem is simply the passive motion of a smooth vortex by the mean flow velocity.

To solve this problem numerically, we consider a smooth grid mapping of the form

$$
\begin{aligned}
x_1\left(\xi_1, \xi_2\right) &= \cos\left(d(r)\theta\right)\xi_1 + \sin\left(d(r)\theta\right)\xi_2, \\
x_2\left(\xi_1, \xi_2\right) &= -\sin\left(d(r)\theta\right)\xi_1 + \cos\left(d(r)\theta\right)\xi_2,
\end{aligned}
\tag{43}
$$

as our model quadrilateral grids (cf. [12]). Here $d(r)$ is defined as

$$
d(r) = \begin{cases} (1 + \cos(\pi r/R))/2 & \text{if } r < R, \\ 0 & \text{otherwise} \end{cases}
$$

with $r = \sqrt{(\xi_1 - \bar{\xi}_1)^2 + (\xi_2 - \bar{\xi}_2)^2}$, and θ is a parameter that measures the maximum skewness of the grid. Note that in case $\theta = 0$, we have a standard

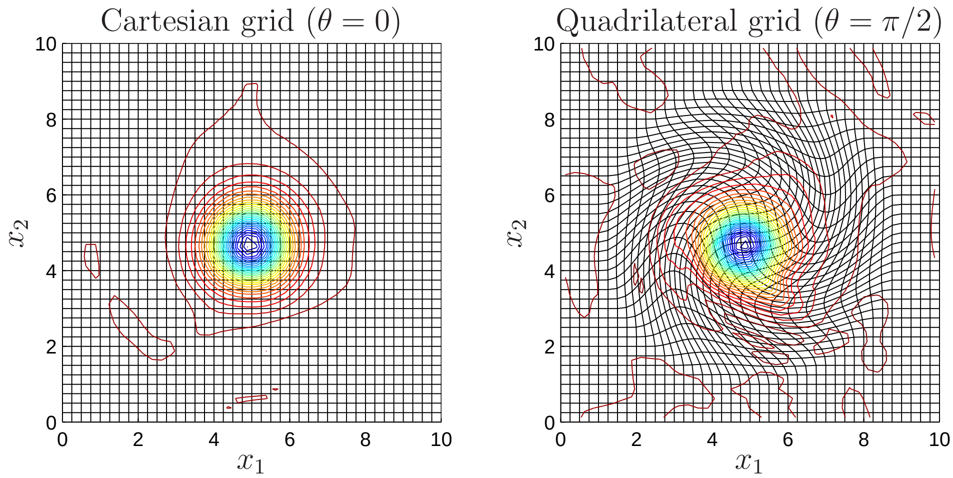

Figure 2: Density contours for the smooth vortex flow computed using a 40×40 mapped grid (43) with the parameters $\theta = 0$ on the left and $\theta = \pi/2$ on the right. Solutions are shown after one time period $t = 10$.

Cartesian grid, and in case $\theta \neq 0$, the grid is rotated in a circular region of radius R about the center $(\bar{\xi}_1, \bar{\xi}_2)$, but is Cartesian elsewhere.

Here, as an example to see how numerical solutions are influenced by the skewness of the grid, we take $\bar{\xi}_1 = 5$, $\bar{\xi}_2 = 5$, $R = 4$, and consider two different instances with $\theta = 0$ and $\pi/2$ in the grid mapping (43), while carrying out the computations. Figure 2 shows the grids and the contours in density after one time period $t = 10$ for runs using a 40×40 grid. Clearly as far as the basic structure of the solution is concerned, our skewed grid result is not as good as the purely Cartesian one, which is as expected however (cf. [12]). Numerical results for a grid refinement study of errors with $\theta = 0$ and $\pi/2$ at time $t = 10$ are presented in Tables 1 and 2, respectively. From the former table (*i.e.*, the Cartesian grid case), we observe essentially a second order convergence rate of the solutions in both the 1- and maximum-norm, while from the latter table (*i.e.*, the skewed grid case), we see a slight degraded of the convergence behavior to be on the average of order 1.42 in the 1-norm, and of order 1.57 in the maximum-norm. The effect of grid mapping to our method on smooth flows is clearly demonstrated by the results shown above. It is certainly desirable to devise a truly second order method on mapped grids, but the work towards this is beyond the scope of this paper.

Note in the above tables $\|E_z\|_{1,\infty} = \|z_{\text{comput}} - z_{\text{exact}}\|_{1,\infty}$ means a numerical error for the state variable z in the discrete 1- and maximum-norm, respectively (cf. [27]). The number in the parenthesis represents the exponent of the base 10, for example, $1.1439(-1)$ stands for 1.1439×10^{-1}. The order of accuracy of a method is computed in a standard way by performing a linear least-squares fit to a sequence of mesh refinement data and take the slope as the order of accuracy of the method. To ensure that our convergence study is not adversely affected by a loss of accuracy near local extrema in the solution, there is no limiter being used in the computations.

4.1.2. Passive interface evolution

We are next concerned with an interface only problem that the exact solution consists of a circular water column evolving in the air with uniform equilibrium pressure $\bar{p} = 10^5$Pa and constant particle velocity $(\bar{u}_1, \bar{u}_2) = (10^3, 10^3)$m/s throughout a quarter annulus domain. Here we take the initial condition that inside the column of radius $r_0 = 0.2$m about the center $(\bar{x}_1, \bar{x}_2) = (0.8, 0.8)$m the fluid is water with the data

$$(\rho, \gamma, \rho_0, \mathcal{B})_{r \le r_0} = \left(10^3\text{kg/m}^3, 4.4, 10^3\text{kg/m}^3, 2.64 \times 10^6 (\text{m/s})^2\right),$$

while outside the column the fluid is air with the data

$$(\rho, \gamma, \rho_0, \mathcal{B})_{r > r_0} = \left(1.2\text{kg/m}^3, 1.4, 1.2, 0\right).$$

Note that despite the simplicity of the solution structure, this problem is one of the popular tests for the numerical validation of a compressible multicomponent flow solver (cf. [34, 49]).

To discretize this quarter-annulus region, we use polar coordinates:

$$\begin{aligned} x_1(\xi_1, \xi_2) &= \xi_1 \cos(\xi_2), \\ x_2(\xi_1, \xi_2) &= \xi_1 \sin(\xi_2), \end{aligned}$$

for $0.5\text{m} \le \xi_1 \le 2.5\text{m}$ and $0 \le \xi_2 \le \pi/2$, see Chapter 23 of [26] for an illustration. Numerical results of the density and pressure obtained using our algorithm with non-reflecting boundary conditions on all sides and a 100×100 grid is shown in Fig. 3, where the 3D surface plots and the cross-section plots along $\xi_2 = \pi/4$ are presented at time $t = 520\mu$s. From the displayed profiles, it is easy to observe the good agreement of the numerical solutions as compared with the exact results. Notice that the computed pressure remains in the correct equilibrium state $\bar{p}$ (to be more accurate, the difference of these two is only on the order of machine epsilon), without any spurious oscillations near the bubble interface. Moreover, the bubble retains its circular shape and appears to be very well located also.

Table 1: An accuracy study for a smooth vortex problem on mapped grids (43) with $\theta = 0$. Discrete 1- and maximum-norm errors in primitive variables are shown after 1 time period $t = 10$.

Mesh size	40×40	80×80	160×160	320×320	Order
$\|E_\rho\|_1$	7.0710(−1)	1.9186(−1)	4.7927(−2)	1.1941(−2)	1.97
$\|E_p\|_1$	8.5264(−1)	2.3594(−1)	5.9209(−2)	1.4721(−2)	1.96
$\|E_{u_1}\|_1$	2.3716(00)	6.1437(−1)	1.5298(−1)	3.8204(−2)	1.99
$\|E_{u_2}\|_1$	1.9377(00)	4.7673(−1)	1.1773(−1)	2.9262(−2)	2.02
$\|E_\rho\|_\infty$	1.4587(−1)	3.8860(−2)	9.5936(−3)	2.3179(−3)	2.00
$\|E_p\|_\infty$	1.8528(−1)	5.0122(−2)	1.2401(−2)	3.0285(−3)	1.98
$\|E_{u_1}\|_\infty$	3.9934(−1)	1.0488(−1)	2.4857(−2)	6.1654(−3)	2.01
$\|E_{u_2}\|_\infty$	2.0948(−1)	5.5860(−2)	1.3506(−2)	3.3386(−3)	2.00

Table 2: An accuracy study for a smooth vortex problem on mapped grids (43) with $\theta = \pi/2$. Discrete 1- and maximum-norm errors in primitive variables are shown after 1 time period $t = 10$.

Mesh size	40×40	80×80	160×160	320×320	Order
$\|E_\rho\|_1$	1.1921(00)	4.1732(−1)	1.6058(−1)	7.0078(−2)	1.36
$\|E_p\|_1$	1.4984(00)	5.3128(−1)	2.1063(−1)	9.3740(−2)	1.33
$\|E_{u_1}\|_1$	2.7085(00)	8.5937(−1)	2.8118(−1)	1.0743(−1)	1.56
$\|E_{u_2}\|_1$	2.3014(00)	7.4990(−1)	2.7248(−1)	1.1608(−1)	1.44
$\|E_\rho\|_\infty$	1.8793(−1)	6.2063(−2)	1.9104(−2)	7.0730(−3)	1.59
$\|E_p\|_\infty$	2.2841(−1)	7.2502(−2)	2.1285(−2)	7.9266(−3)	1.63
$\|E_{u_1}\|_\infty$	4.0762(−1)	1.3207(−1)	4.2383(−2)	1.5737(−2)	1.57
$\|E_{u_2}\|_\infty$	2.6456(−1)	9.0362(−2)	2.7416(−2)	1.2385(−2)	1.50

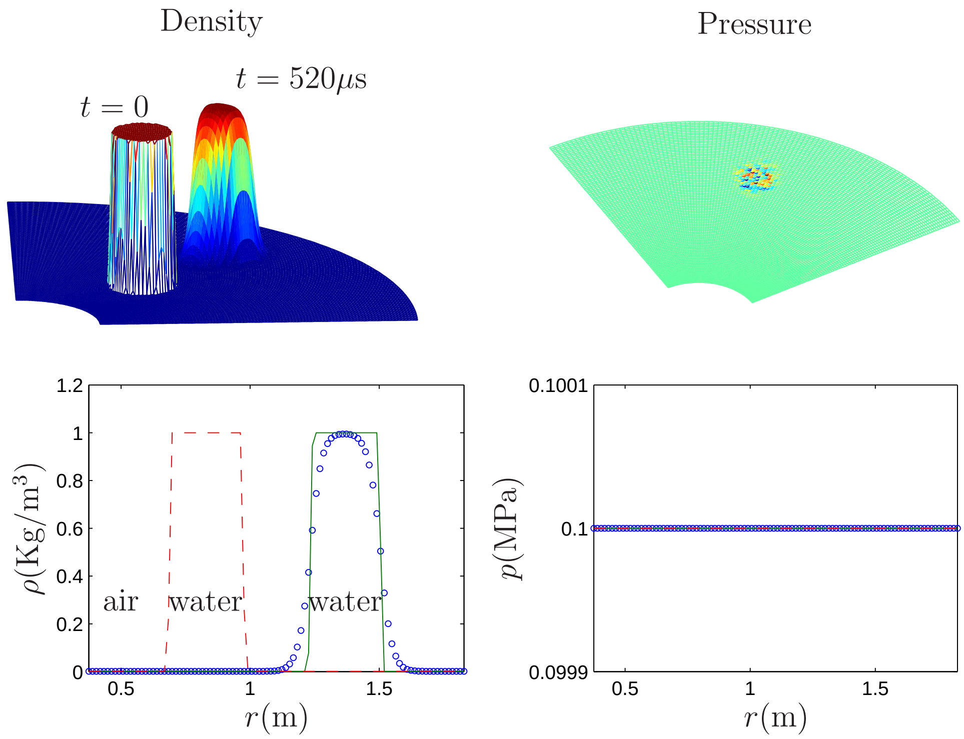

Figure 3: Surface (top) and cross-sectional (bottom) plots of the density and pressure for an interface only problem in a quarter annulus. Cross-sectional plots are displayed along the line $\xi_2 = \pi/4$, where the solid line is the exact solution, and the dashed line is the initial condition at the time $t = 0$.

4.1.3. Blast wave in radial geometry

To validate our numerical method further, we are interested in a radially symmetric flow where the computed solutions in two space dimensions can be in comparison to the one-dimensional results. In this test, we take a quarter of a circular domain of radius $r_0 = 1$m, and use the following two-phase (gas-liquid) flow data for experiments in which, in the gas phase, the state variables are

$$(\rho, p, \gamma, \rho_0, \mathcal{B}) = \left(1250\mathrm{kg/m^3}, 10^9\mathrm{Pa}, 1.4, 1.2\mathrm{kg/m^3}, 0\right)$$

and

$$(\rho, p, \gamma, \rho_0, \mathcal{B}) = \left(1.2\mathrm{kg/m^3}, 10^5\mathrm{Pa}, 1.4, 1.2\mathrm{kg/m^3}, 0\right)$$

if $r < r_1$ and $r_2 < r \leq r_0$, respectively, while in the liquid phase they are

$$(\rho, p, \gamma, \rho_0, \mathcal{B}) = \left(10^3\mathrm{kg/m^3}, 10^5\mathrm{Pa}, 4.4, 10^3\mathrm{kg/m^3}, 2.64 \times 10^6(\mathrm{m/s})^2\right),$$

if $r_1 < r \leq r_2$. Here we have $r_1 = 0.2$m, $r_2 = 0.7$m, and $r = \sqrt{x_1^2 + x_2^2}$.

We note that initially all the fluid components are in a resting state with zero total velocity, but due to the pressure difference between the fluids at $r = r_1$, breaking of the inner circular membrane occurs instantaneously, yielding an outward-going shock wave in liquid, an inward-going rarefaction wave in gas, and a material interface lying in between that separates the gas and liquid. As times go along, the inward-going wave would be reflected from the geometric center that generates a new outward-going wave and induces the subsequent interaction of waves. In the meantime, the outward-going shock wave would be collided with the outer gas-liquid interface at $r = r_2$ that results in a wave pattern consisting of a transmitted shock wave, an interface, and a reflected rarefaction wave. At a later time, the transmitted shock wave would be reflected from the boundary of the domain.

To solve this problem numerically, we are interested in a mapped grid approach proposed by Calhoun *et al.* [11] in that a grid point (ξ_1, ξ_2) in the computational domain $[0,1] \times [0,1]$ would be mapped to a grid point (x_1, x_2) in the current quarter-circular domain, see Fig. 4 for an example of such a quadrilateral grid. Figure 5 shows the contours for the density, radial velocity (defined as $\bar{u} = \sqrt{u_1^2 + u_2^2}$), and pressure, at three stopping times $t = 150$, 360, and 520μs, where the test has been carried out by using solid wall boundary conditions on all sides with a 100×100 grid in the computational domain, see [26] for the detailed discussion on how to impose this boundary condition in a numerical method. From the figure, we observe good resolution of the solution structure (*i.e.*, both the shock and interface remain circular and appear to be very well located) after the breaking of the membrane and also the interaction of the shock, the outer interface, and the boundary. The scatter plots presented in Fig. 6 provide the quantitative comparison of our two-dimensional results to the "true" solution obtained from solving the one-dimensional model with appropriate source terms for the radial symmetry using the high-resolution method with 1000 mesh points in a unit length domain (cf. [35]). It is clear that our results agree quite well with the "true" solutions at all the selected times, and are free of spurious oscillations in the pressure near the inner and outer interfaces before and after the various wave interactions.

4.1.4. Moving cylindrical vessel

Our next example on a circular geometry concerns a moving cylindrical vessel problem studied by Banks *et al.* [5] in that inside the circle of radius

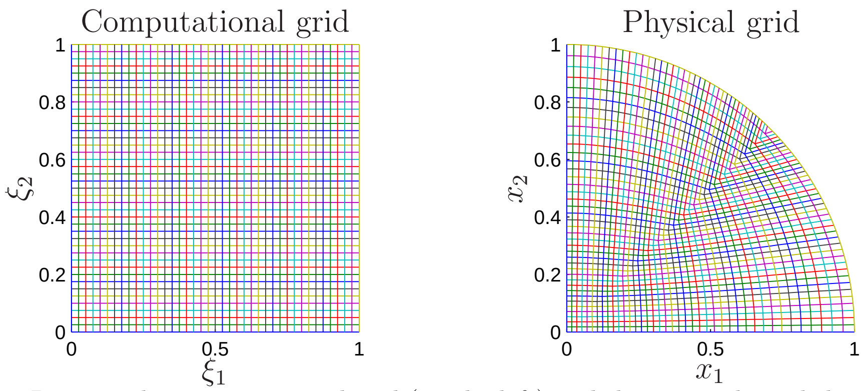

Figure 4: Rectangular computational grid (on the left) and the mapped quadrilateral grid (on the right) in a quarter-circular domain.

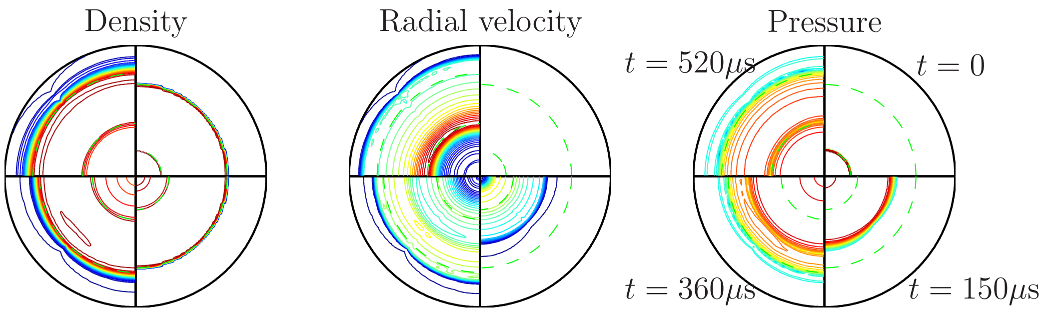

Figure 5: Contours of the density, radial velocity, and pressure for a two-phase (gas-liquid) radially symmetric problem in a quarter of a circular domain. Solutions are plotted in a clockwise manner at times $t = 0$, 150, 360, and 520μs, where the dashed line is the approximate location of the interface.

$r_0 = 0.8$ about the origin, there is a planar material interface located initially at $x_1 = 0$ that separates air on the left with the state variables

$$(\rho, u_1, u_2, p, \gamma, \rho_0, \mathcal{B}) = (1, -1, 0, 1, 1.4, 1, 0)\,,$$

and helium on the right with the state variables

$$(\rho, u_1, u_2, p, \gamma, \rho_0, \mathcal{B}) = (0.138, -1, 0, 1, 1.67, 0.138, 0)\,.$$

Note that in this set up we have imposed a uniform flow velocity $(u_1, u_2) = (-1, 0)$ throughout the domain, and so we are in the frame of the vessel moving with speed one in the x_1-direction.

To find an approximate solution of this problem, we use a similar mapped grid as illustrated in Fig. 4, but is now defined in the whole circular region.

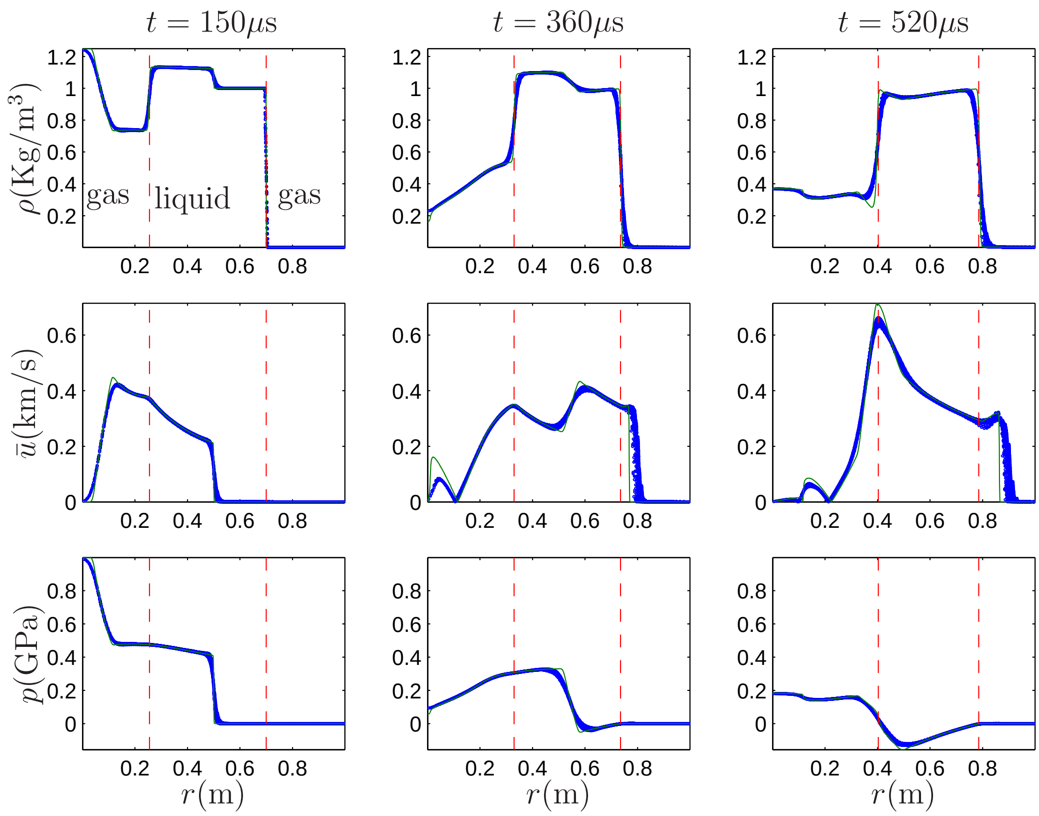

Figure 6: Scatter plots of the results for the run shown in Fig. 5, where the solid line is the "true" solution obtained from solving the one-dimensional model with appropriate source terms, and the dashed line is the approximate location of the interface.

Figure 7 gives results of a run with a 800×800 grid, where numerical Schlieren images and pseudo-color plots of pressure are shown at four different times $t = 0.25$, 0.5, 0.75, and 1.0. From the figure, it is easy to see that due to the impulsive motion of the vessel a rightward-going shock wave and a leftward-going rarefaction wave emerge from the left- and right-side boundary, respectively. Subsequently, these two waves would be interacting with the material interface that leads to collision of various transmitted and reflected waves. When we compare our results with those ones appeared in the literature (cf. [5, 49]), as far as the global wave structures are concerned, we notice good qualitative agreement of the solutions. To check the quantitative information of our computed solutions, Fig. 8 compares the cross section of the results for the same run along the circular boundary with the results obtained using a Cartesian grid embedded boundary method [39]. The close agreement between the mapped grid and Cartesian grid results in the shock waves and material interfaces are clearly observed.

4.1.5. Shock-bubble interaction in a nozzle

As an example to show how our algorithm works on shock waves in a more general two-dimensional geometry, we are interested in a shock-bubble interaction problem in a nozzle. For this problem, the shape of the nozzle is described by a flat curve

$$x_2^t = 1\text{m}$$

on the top, and by the witch of Agnesi

$$x_2^b\left(x_1\right) = \frac{8a^3}{x_1^2 + 4a^2}$$

on the bottom for $a = 0.2$m and $-2\text{m} \le x_1 \le 3\text{m}$. We use the initial condition that is composed of a planarly rightward-going Mach 1.422 shock wave located at $x_1 = -1.8$m in liquid traveling from left to right, and a stationary gas bubble of radius $r_0 = 0.2$m and center $(\bar{x}_1, \bar{x}_2) = (-1, 0.5)$m in the front of the shock wave. Inside the gas bubble, we have the data

$$(\rho, u_1, u_2, p) = \left(1.2\text{kg/m}^3, 0, 0, 10^5\text{Pa}\right),$$

while outside the gas bubble where the fluid is liquid, we have the preshock state

$$(\rho, u_1, u_2, p) = \left(10^3\text{kg/m}^3, 0, 0, 10^5\text{Pa}\right),$$

and the postshock state

$$(\rho, u_1, u_2, p) = \left(1.23 \times 10^3\text{kg/m}^3,\ 432.69\text{m/s}, 0,\ 10^9\text{Pa}\right).$$

Here the numerical values for the material-dependent parameters of the gas- and liquid-phase in the equation of state, *i.e.*, γ, ρ_0, and $\mathcal{B}$, are taken the same as in Section 4.1.3 for the radially symmetric problem.

In carrying out the computation, we consider a body-fitted quadrilateral grid with the mapping function

$$\begin{aligned} x_1\left(\xi_1, \xi_2\right) &= \xi_1, \\ x_2\left(\xi_1, \xi_2\right) &= x_2^b\left(\xi_1\right)\left(\frac{\xi_2^t - \xi_2}{\xi_2^t - \xi_2^b}\right) \end{aligned} \tag{44}$$

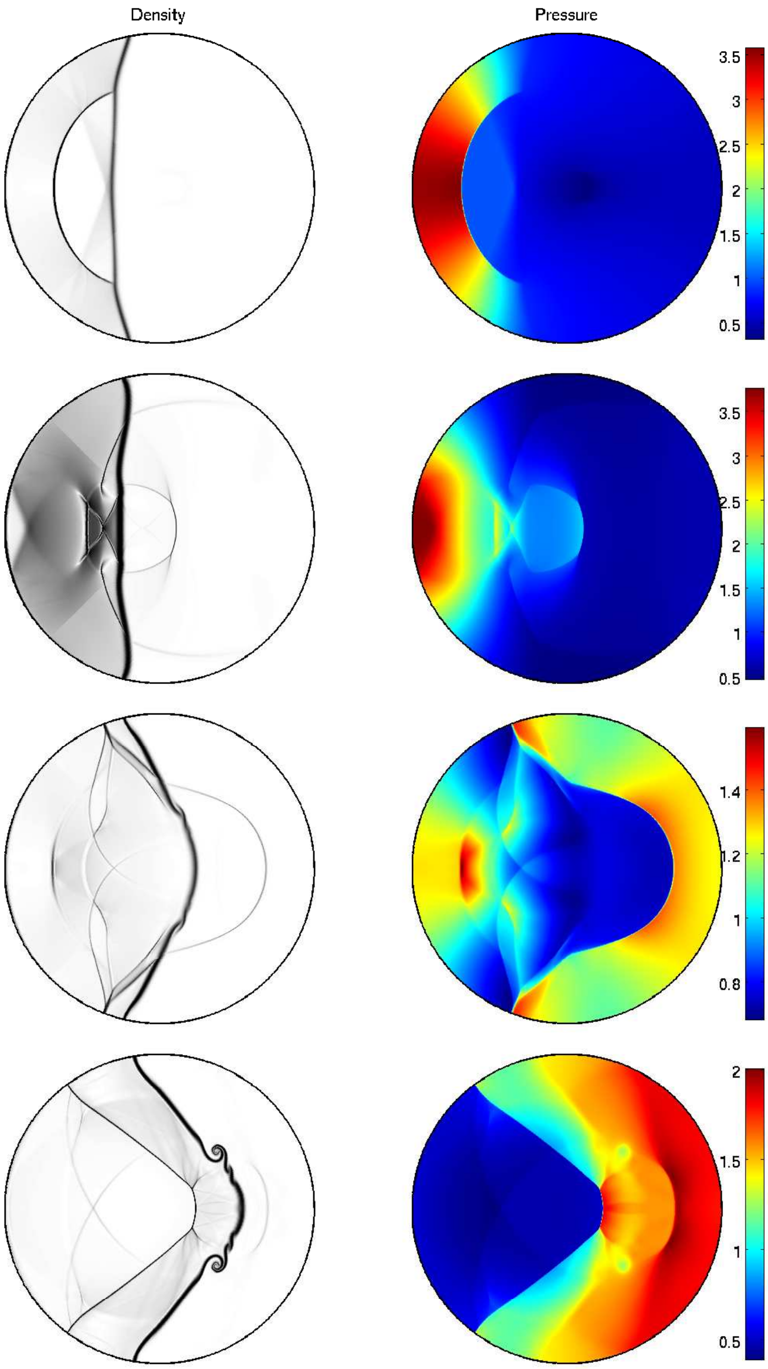

Figure 7: Numerical Schlieren images (on the left) and pseudo colors of pressure (on the right) for an impulsively driven cylinder containing an air-helium material interface. Solutions from top to bottom are at times $t = 0.25$, 0.5, 0.75, and 1.0.

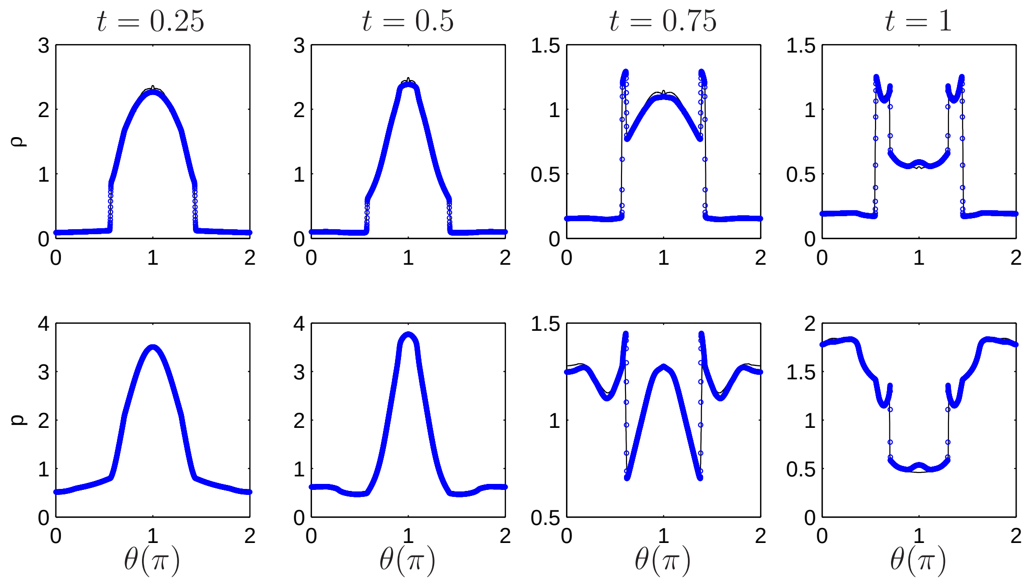

Figure 8: Cross-sectional plots of the results for the moving vessel run shown in Fig. 7 along the circular boundary, where the solid lines are results obtained using a Cartesian grid embedded boundary method [39] with the same grid size.

for $-2\text{m} \leq \xi_1 \leq 3\text{m}$, $0 \leq \xi_2 \leq 1\text{m}$, $\xi_2^b = 0$, and $\xi_2^t = 1\text{m}$, see Fig. 9 for an illustration with a 100×20 mesh cells. The boundary conditions are the supersonic inflow on the left-hand side, the non-reflecting on the right-hand side, and the solid wall on the remaining sides. In Fig. 10, we show the schlieren images and pseudo colors of pressure at six different times $t = 0.3$, 0.5, 0.7, 1.2, 1.6, and 2.5ms obtained using a 1000×200 grid. From the figure, it is easy to see that after the passage of the shock to the gas bubble, the upstream wall begins to spall across the bubble, yielding a refracted air shock traveling within it until its first reflection on the downstream bubble wall. Noticing that this upstream bubble wall would be involute eventually to form a jet which subsequently crosses the bubble and sends an intense blast wave out into the surrounding liquid. In the meantime, the incident shock wave along the bottom curved boundary would be diffracted into a simple Mach reflection. To check the quantitative information of the solutions, Fig. 11 compares the cross section of the results along the $\xi_2 = 0.5\text{m}$ line with the same method but with a finer 2000×400 grid. Convergence of our computed solutions to the correct weak ones is clearly observed. In addition, Fig. 12 compares the cross section of the results for the same run along the

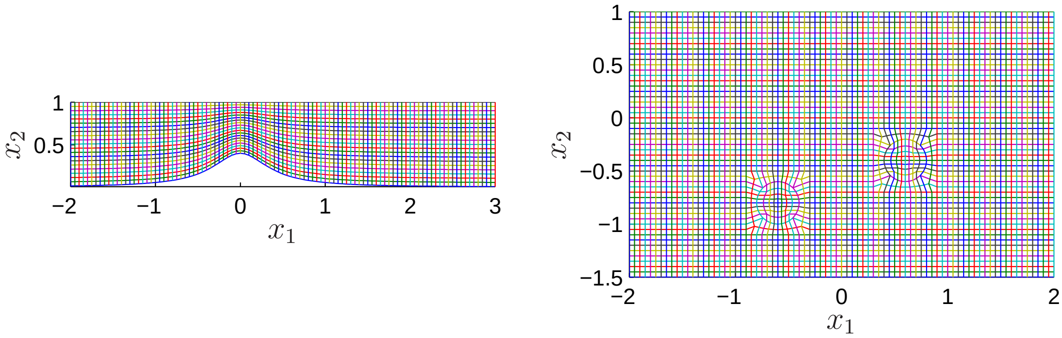

Figure 9: On the left, a sample quadrilateral grid in a nozzle, and on the right, a quadrilateral grid in a rectangular region with circular obstacles.

bottom boundary with the results obtained using a Cartesian grid embedded boundary method [39]. The close agreement between the mapped grid and Cartesian grid results are seen also.

4.1.6. Underwater explosion with circular obstacles

Our next example for problems in more general geometries is an underwater explosion flow with circular obstacles, see [28] for a similar computation but with a square obstacle. In this test, the physical domain is a rectangular region of size $([-2, 2] \times [-1.5, 1])\text{m}^2$ in which inside the domain there are two circular obstacles, denoted by b_1 and b_2, with the centers $(\bar{x}_1^{b_1}, \bar{x}_2^{b_1}) = (-0.6, -0.8)$m and $(\bar{x}_1^{b_2}, \bar{x}_2^{b_2}) = (0.6, -0.4)$m, respectively, and of the same radius $r_{b_1} = r_{b_2} = 0.2$m. The initial condition we consider is composed of a horizontal air-water interface at $x_2 = 0$ and a circular gas bubble in water that lies below the interface. Here all the fluid components are at rest initially. When $x_2 \geq 0$, the fluid is air with the state variables

$$(\rho, p) = \left(1.2\text{kg/m}^3, 10^5\text{Pa}\right),$$

and when $x_2 < 0$ and $r < r_0$, the fluid is gas with the state variables

$$(\rho, p) = \left(1250\text{kg/m}^3, 10^9\text{Pa}\right).$$

Now, in the remaining region where the obstacles do not belong to, the fluid is water with the states

$$(\rho, p) = \left(10^3\text{kg/m}^3, 10^5\text{Pa}\right).$$

As before, the radial distance r is defined by $\sqrt{(x_1 - \bar{x}_1)^2 + (x_2 - \bar{x}_2)^2}$, and we have $r_0 = 0.12$m and $(\bar{x}_1, \bar{x}_2) = (0, -0.9)$m in the current case. The

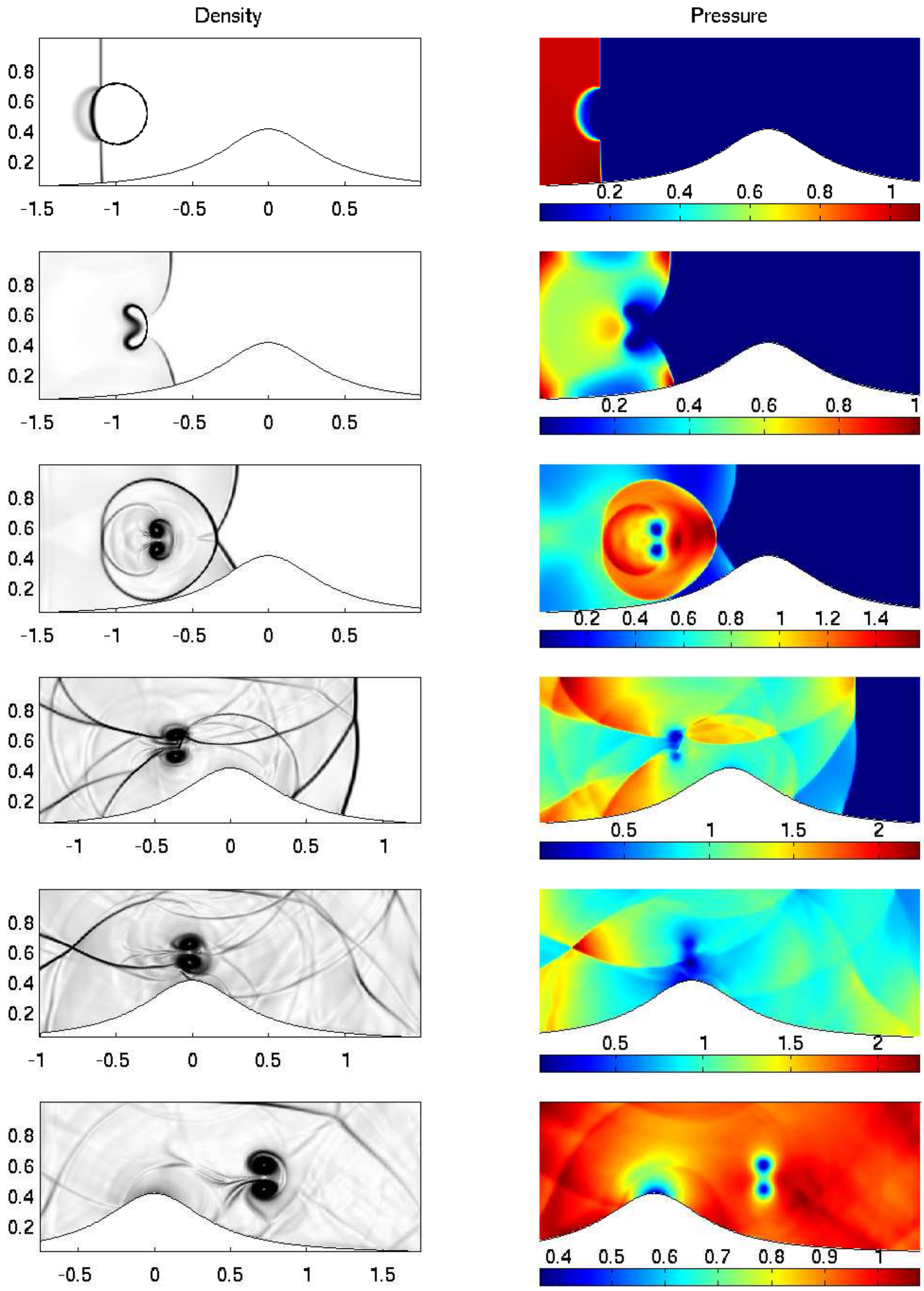

Figure 10: Numerical Schlieren images (on the left) and pseudo colors of pressure (on the right) for a planar shock wave in liquid over a circular gas bubble in a nozzle. Solutions from top to bottom are at times $t = 0.3$, 0.5, 0.7, 1.2, 1.6, and 2.5ms, and are plotted in a close neighborhood of the gas bubble.

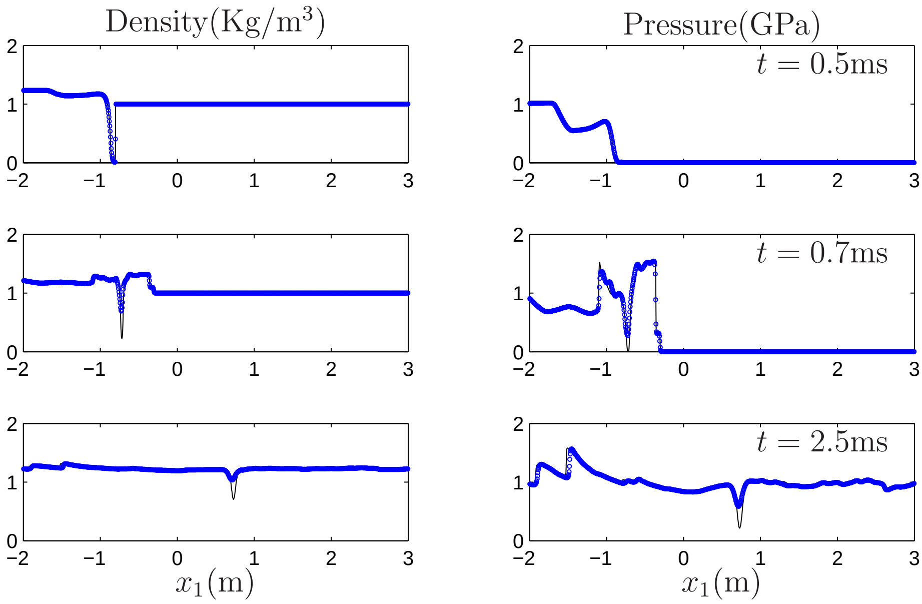

Figure 11: Cross-sectional plots of the results at the selected times $t = 0.5$, 0.7, and 2.5ms along the $\xi_2 = 0.5$m line, where the solid lines are results obtained using the same method but with a finer 2000×400 grid.

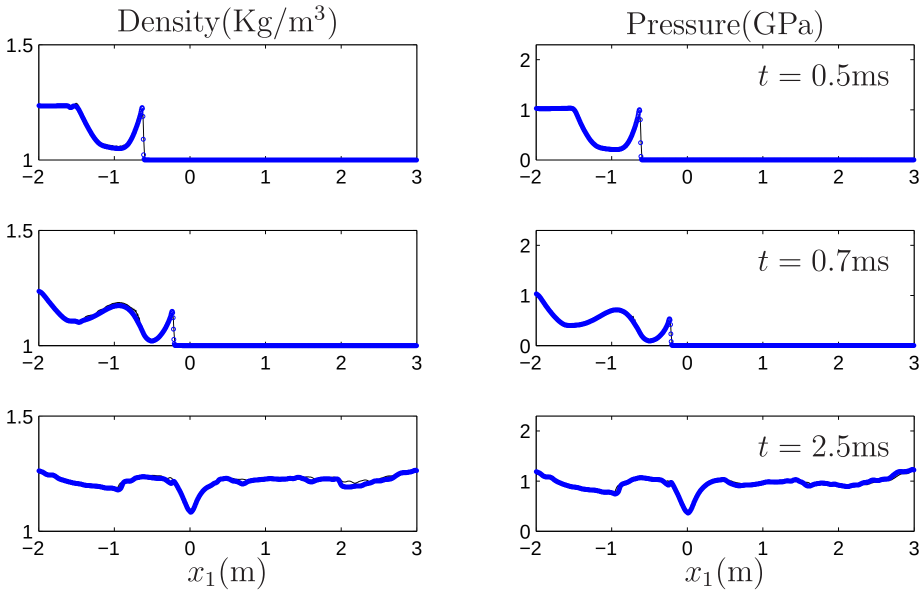

Figure 12: Cross-sectional plots of the results at the selected times $t = 0.5$, 0.7, and 2.5ms along the bottom boundary, where the solid lines are results obtained using using a Cartesian grid embedded boundary method [39] with the same grid size.

material-dependent quantities for the gas- and liquid-phase are the same as in the previous tests.

We solve this problem using a mapped quadrilateral grid that has the circular obstacles included in the domain as illustrated in Fig. 9, see [11] for the detailed construction. Figure 13 gives the numerical results of the density and pressure at six different times $t = 0.24$, 0.4, 0.8, 1.2, 2.0, and 3.0ms, obtained using a 800×500 grid with the non-reflecting boundary on the top, and the solid wall boundary on the remaining sides. From the figure, it is easy to observe that in the early stage of the computation the flow field is essentially radial symmetry. Soon after the outward-going shock wave is reaching at the left obstacle and then the right obstacle, a reflected shock wave results from each of the shock-obstacle collisions. As time goes on, these reflected shock waves would affect the structure of the gas bubble, and that induces numerous other wave-wave and wave-obstacle interactions at the later time. We note that when the outward-going shock is approaching at the air-water interface, we have a typical heavy-to-light shock-contact interaction, and the resulting wave pattern after the interaction would consist of a transmitted shock wave, an accelerated air-water interface, and a reflected rarefaction wave. In Fig. 13, the cross section of the results are drawn along the line $\xi_1 = 0$ at the selected times.

For practical applications, it is important to know how the effect of the impinging waves on the obstacles. As a measure of that, we compute the surface pressure force exerted on the boundary of the obstacle by integrating the following line integral numerically:

$$F_i(t) = -\oint_{\partial b_i} p(t)\ dl$$

for the obstacle b_i, $i = 1, 2$. Figure 14 gives the results for that until the time $t = 3$ms, where a grid sequence, $2^i \times (200, 125)$ for $i = 0, 1, 2$, is used in the test to show the convergence behavior of the solution. A comparison between the mapped and Cartesian grid results on this pressure force history on the obstacles is shown in Fig. 15 where the good agreement of the solutions is observed again. From these graphs, the existence of positive pressure force is clearly seen in some time intervals, which mean the negative value of the pressure around the obstacles. This is, however, permitted in the current model with the stiffened gas equation as long as the pressure stays within the region of the thermodynamic stability of the flow.

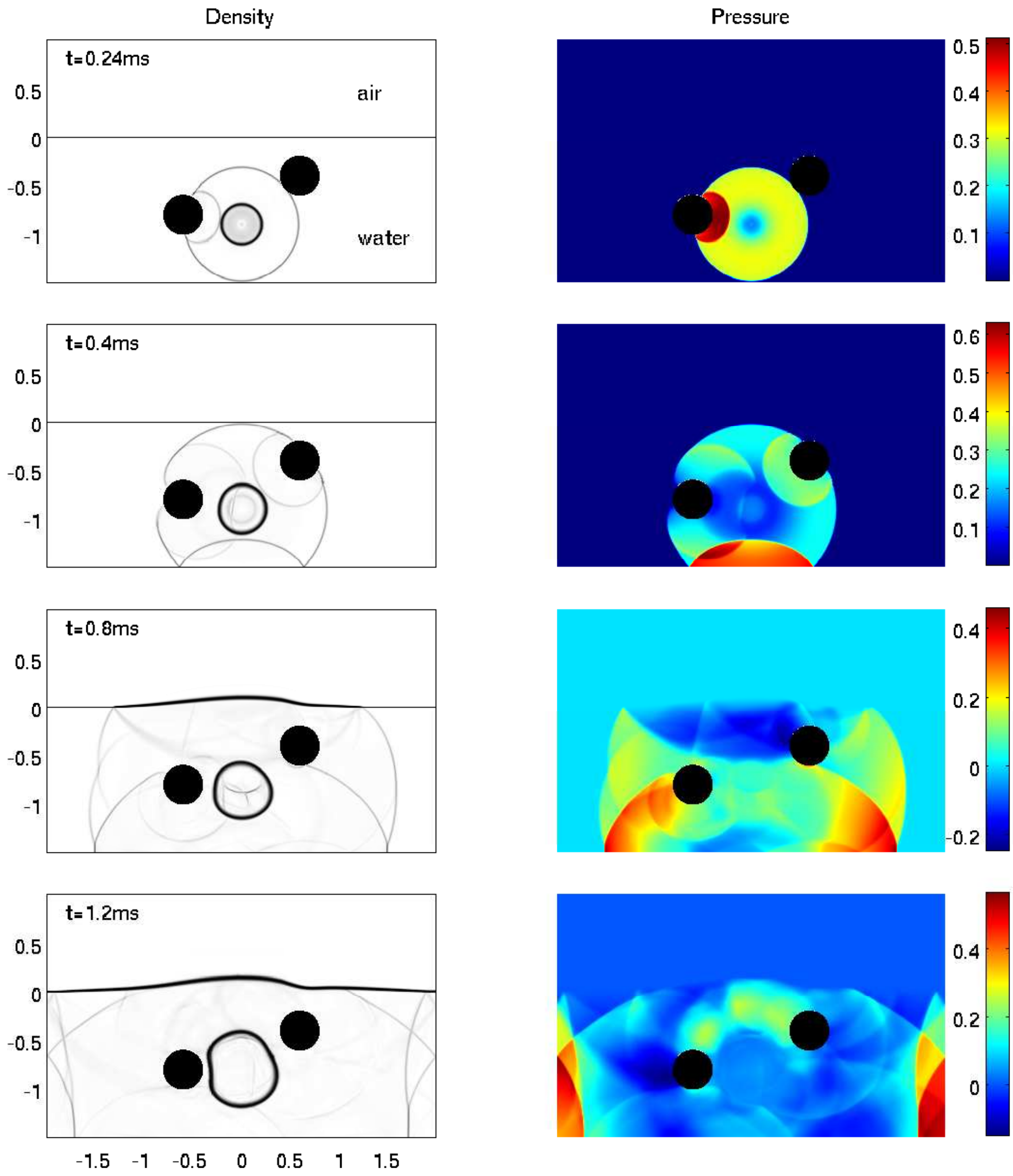

Figure 13: Numerical Schlieren images (on the left) and pseudo colors of pressure (on the right) for an underwater explosion problem with two circular obstacles. Solutions are shown at six different times $t = 0.24$, 0.4, 0.8, 1.2, 2.0, and 3.0ms, where a 800×500 grid was used in the computation.

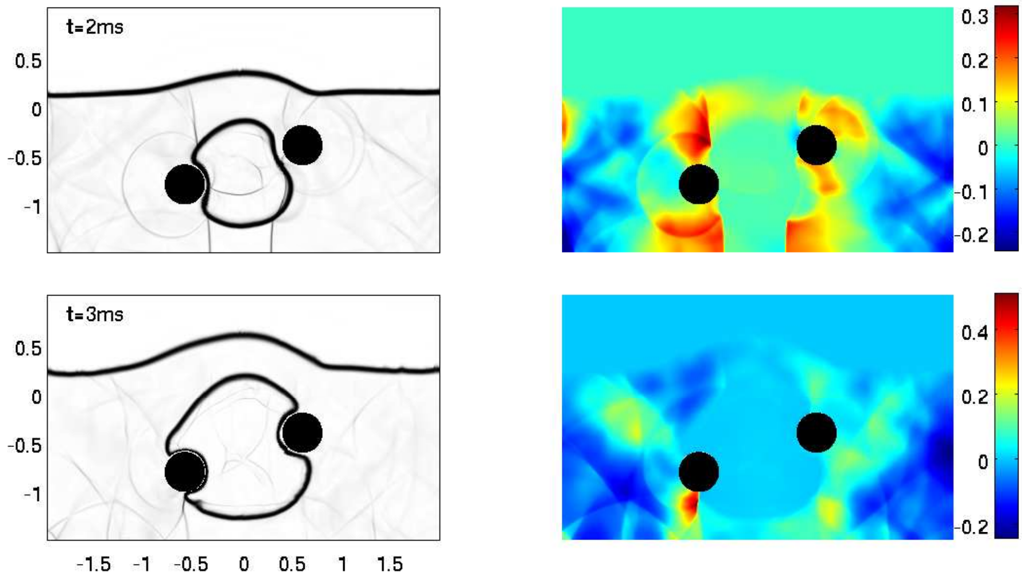

Figure 12: Continued.

4.1.7. Water wave breaking problem

To see how our algorithm works on a weakly compressible low speed flow, we consider the simulation of a gravity-included water wave breaking problem studied by Golay and Helluy [15]. In this test, initially, we have a rightward-going stable solitary water wave in an air with a crest height 0.6m over the still water level traveling on a flat bottom from the left toward a slope-like reef on the right of the form

$$x_2^b\left(x_1\right) = -1 + \frac{1}{15}\left(x_1 - 5.225\right)$$

for $-5\text{m} \leq x_1 \leq 22\text{m}$ and $-1\text{m} \leq x_2 \leq 2\text{m}$, see Fig. 16 for an illustration of the basic structure of the physical states in filled contours. Note that in practice this solitary water wave can be constructed by the Tanaka method [43], and conveniently this can be done by making use of the computer program posted at the web-site http://helluy.univ-tln.fr/soliton.htm (cf. [18]).

It should be mentioned, for this problem, the constitutive laws for the water and air are assumed to satisfy the stiffened gas equation of state as before, while the algorithm is based on the balance law (30) together with (33) as the model equations for the computations. Here a standard time-splitting

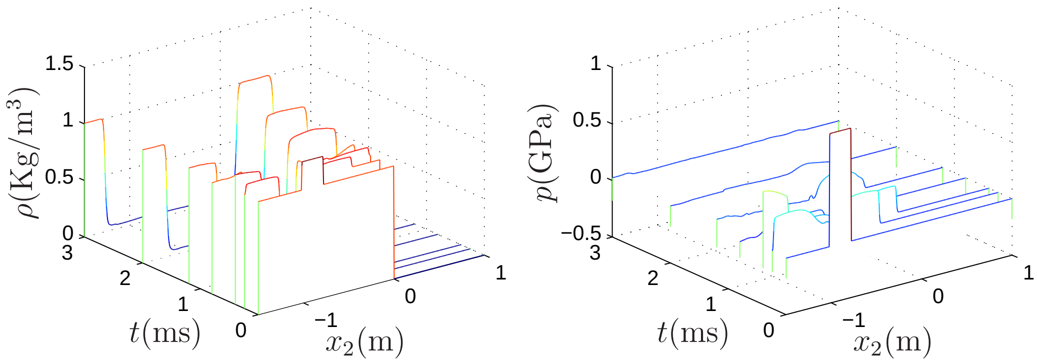

Figure 13: Cross-sectional plots of the results for the underwater explosion run shown in Fig. 13 along the $\xi_1 = 0$ line.

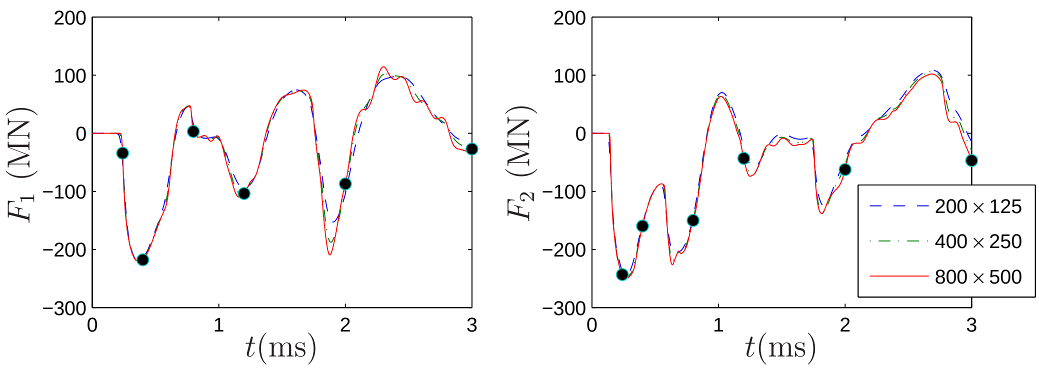

Figure 14: Convergence study of the time history of the pressure force on the circular obstacles for the underwater explosion problem. The filled circles in the graph are the results at the selected times shown in Fig. 13.

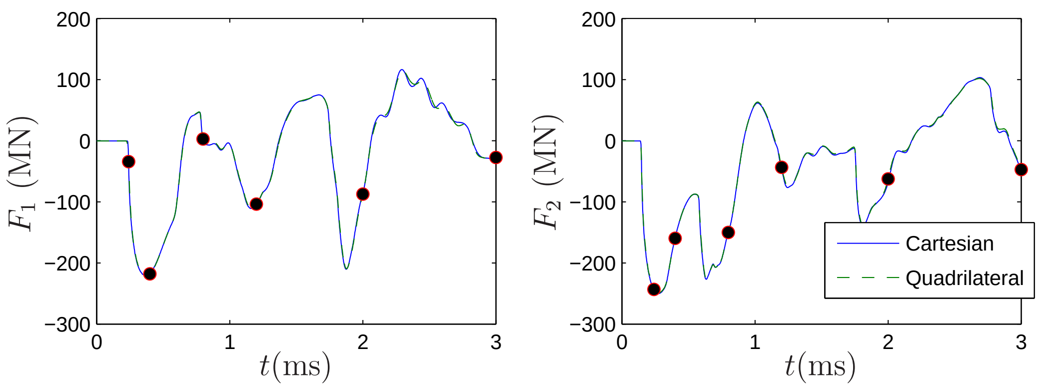

Figure 15: Comparison of the mapped and Cartesian grid results for the the pressure force on the circular obstacles in an underwater explosion problem. The graphs are displayed in the same manner as in Fig. 14.

version of the method is considered to deal with the source terms (cf. [27]), and the domain is discretized similar to the nozzle flow case before by the mapping function as

$$x_1 = \xi_1, \qquad x_2 = \begin{cases} \xi_2 & \xi_1 \le 5.225 \\ x_2^b(\xi_1)\left(\xi_2^t - \xi_2\right) / \left(\xi_2^t - \xi_2^b\right) & \xi_1 > 5.225 \end{cases}$$

for $-5\text{m} \le \xi_1 \le 22\text{m}$, $-1\text{m} \le \xi_2 \le 2\text{m}$, $\xi_2^b = -1\text{m}$, and $\xi_2^t = 2\text{m}$. Figure 17 shows the pseudo-color images of the computed density at four different times $t = 2$, 4, 4.5, and 5s with a 1800×200 mesh cells. The breaking of the solitary wave is clearly seen after the passage of the slanted reef. As far as the global wave pattern is concerned, our body-fitted mapped grid result is in qualitative agreement with the unstructured grid result reported in [15]. It should be noted however that because the the flow speed is typically much less than the speed of sound of the water, to carry out the computation using the explicit method as proposed here, we would have a severe time step restriction due to the CFL condition for stability, yielding difficulties as the lack of robustness of the method, see [8] and the references therein for more discussions.

4.2. Three-dimensional case

4.2.1. Spherical blast wave

To test our mapped grid algorithm for problems in three dimensions, we begin by considering a blast wave problem inside a unit ball. We want to use a hexahedral grid of the type shown in Fig. 18 for the computation (cf. [11]). As for the initial condition, similar to the two-dimensional problem in a circle, see 4.1.3, the velocity of the flow is zero everywhere, and inside a sphere of radius 0.2m centered at $\bar{x}_1 = \bar{x}_2 = 0$, $\bar{x}_3 = -0.4\text{m}$, the fluid phase is gas with data

$$(\rho, p, \gamma, \rho_0, \mathcal{B}) = \left(1250\text{kg/m}^3, 10^9\text{Pa}, 1.4, 1.2\text{kg/m}^3, 0\right)$$

while outside of this sphere, the fluid phase is liquid with data

$$(\rho, p, \gamma, \rho_0, \mathcal{B}) = \left(10^3\text{kg/m}^3, 10^5\text{Pa}, 4.4, 10^3\text{kg/m}^3, 2.64 \times 10^6(\text{m/s})^2\right),$$

Note that as in [11] this sphere is offsetted from the center of the ball, leading to a more interesting solution structure than the radially symmetric one considered in Section 4.1.3.

Here we carry out the computation in a quarter ball with a $75 \times 75 \times 150$ grid. At each boundary of the computational domain, we use solid wall boundary conditions. For comparison, we also compute the solution in a two-dimensional disk with a finer 300×600 grid using the two-dimensional model (30) with the source term (31) for the axisymmetric. Figure 19 shows a single slice of the three-dimensional computed density and pressure together with the two-dimensional solution at four different times $t = 0.2$, 0.4, 0.6, and 1.0ms. At the early stage of the calculations, the global structure of the shock wave and the material interface agree quite well between the three-dimensional solutions and the fine-grid axisymmetric results. But, it begins to deviate at a later time when more complex wave interactions set on. This is of no surprise, however, because when such a scenario occurs, it is required to use a finer grid to better resolve the solutions (cf. [48]).

4.2.2. Shock wave over two spherical dispersed phases a nozzle

Finally, we are concerned with the simulation of a shock wave in liquid over two disperse phases in a three-dimensional nozzle. For this problem, we consider the initial condition that is composed of a planarly rightward-going shock wave in water traveling at $x_1 = 0.1$m from left to right, and two stationary spherical disperse phases of radius $r_0 = 0.2$m located at $(\bar{x}_1, \bar{x}_2, \bar{x}_3) = (0.5, 0, 0)$m and $(1.5, 0, 0.3)$m on the right of the shock wave. For both the shock wave and the material quantities in the background fluid, the water, we take the same data as employed in Section 4.1.5. For the disperse phase at $x_1 = 0.5$m, the fluid is gas with the data

$$(\rho, \gamma, \rho_0, \mathcal{B}) = \left(50\text{kg/m}^3, 1.4, 50\text{kg/m}^3, 0\right),$$

and for the disperse phase at $x_1 = 1.5$m, the fluid is aluminum with data

$$(\rho, \gamma, \rho_0, \mathcal{B}) = \left(2785\text{kg/m}^3, 3, 2785\text{kg/m}^3, 2.84 \times 10^7 (\text{m/s})^2\right).$$

Note that this gives us an example that involves three phases (water, gas, and solid) in the problem formulation. In carrying out the computations below, the boundary conditions we used are supersonic inflow on the left, non-reflecting on the right faces, and solid wall on the remaining top, bottom, front, and back faces.

We solve this problem using a hexahedral grid of the type shown in Fig. 18. Numerical results of a sample run using a $240 \times 160 \times 80$ grid is shown in Fig. 20. Here pseudo-colors of the density and pressure are plotted at three different slice planes at times $t = 0.2$, 0.6, 1.0, 1.2ms. We again do not observe any spurious oscillations in the computed pressure near both the water-gas and water-solid interfaces. This gives further evidence of the viability of the algorithm to practical problems.

5. Conclusion

We have presented a simple mapped-grid approach for the numerical resolution of compressible multiphase problems with a stiffened gas equation of state in general two- and three-dimensional geometries. The algorithm uses a generalized coordinate formulation of model equations that is devised to ensure a consistent approximation of the energy equation near the numerical-induced smeared material interfaces, and an easy computation of the pressure from the equation of state. A standard finite-volume method based on wave propagation viewpoint is employed to solve the proposed multiphase flow model with the dimensional-splitting technique incorporated for an efficient implementation of the method to multidimensional problems. Several calculations are presented with an HLL-type approximate Riemann solver that show accurate results obtained using the method without introducing any spurious oscillations in the pressure near the interfaces. Numerical results presented in this paper demonstrate clearly the feasibility of the approach for a reasonable class of multiphase problems in both two and three dimensions with complex geometries. One of the ongoing works is to extend this approach further to moving mesh methods and to problems with complex moving geometries.

Acknowledgement

This work was supported in part by a French/Taiwan program ORCHID: Grant of National science council of Taiwan NSC 97-2911-1-002-015 and by National Science Council of Taiwan Grant 96-2115-M-002-008-MY3.

References

[1] R. Abgrall. How to prevent pressure oscillations in multicomponent flow calculations: a quasi conservative approach. *J. Comput. Phys.*, 125:150–160, 1996.

[2] R. Abgrall, B. Nkonga, and R. Saurel. Efficient numerical approximations of compressible multi-material flow for unstructured meshes. *Computers and Fluids*, 32(4):571–605, 2003.

[3] G. Allaire, S. Clerc, and S. Kokh. A five-equation model for the simulation of interface between compressible fluids. *J. Comput. Phys.*, 181:577–616, 2002.

[4] D. A. Anderson, J. C. Tannehill, and R. H. Pletcher. *Computational Fluid Mechanics and Heat Transfer*. McGraw-Hill, New York, 1984.

[5] J. W. Banks, D. W. Schwendeman, A. K. Kapila, and W. D. Henshaw. A high-resolution Godunov method for compressible multi-material flow on overlapping grids. *J. Comput. Phys.*, 223:262–297, 2007.

[6] P. Batten, N. Clarke, C. Lambert, and D. Causon. On the choice of wave speeds for the HLLC Riemann solvers. *SIAM J. Sci. Comput.*, 18:1553–1570, 1997.

[7] J. U. Brackbill, D. B. Kothe, and C. Zemach. A continuum method for modeling surface tension. *J. Comput. Phys.*, 100:335–354, 1992.

[8] B. Braconnier, J.-J. Hu, Y.-Y. Niu, B. Nkonga, and K.-M. Shyue. Numerical simulations of low mach compressible two-phase flows: Preliminary assessment of some basic solution techniques. *ESAIM: Proceedings*, 28:118–135, 2009.

[9] D. L. Brown. An unsplit Godunov method for systems of conservation laws on curvilinear overlapping grids. *Math. Comput. Modelling*, 20:29–48, 1994.

[10] D. A. Calhoun, C. Helzel, and R. J. LeVeque. A finite volume grid for solving hyperbolic problems on the sphere. In *Hyperbolic Problems: Theory, Numerics, Applications*, pages 355–362. Springer-Verlag, 2008.

[11] D. A. Calhoun, C. Helzel, and R. J. LeVeque. Logically rectangular grids and finite volume methods for PDEs in circular and spherical domains. *SIAM Review*, 50(4):723–752, 2008.

[12] D. A. Calhoun and R. J. LeVeque. An accuracy study of mesh refinement on mapped grids. In *Adaptive mesh refinement, theory, and applications: proceedings of the Chicago Workshop on Adaptive Mesh Refinement Methods, Sept. 3-5, 2003*, Lecture note in computational science and engineering, pages 91–102. Springer, New York, 2005.

[13] J. Cheng and C.-W. Shu. A high order ENO conservative Lagrangian type scheme for the compressible Euler equations. *J. Comput. Phys.*, 227:1567–1596, 2007.

[14] R. Courant and K. O. Friedrichs. *Supersonic Flow and Shock waves.* Wiley-Interscience, New York, 1948.

[15] F. Golay and P. Helluy. Numerical schemes for low Mach wave breaking. *Int. J. Comput. Fluid Dyn.*, 21:69–86, 2007.

[16] F. Harlow and A. A. Amsden. *Fluid Dynamics.* Los Alamos National Laboratory, Los Alamos, NM, 1971. Monograph LA-4700.

[17] A. Harten, P. D. Lax, and B. van Leer. On upstream differencing and Godunov-type schemes for hyperbolic conservation laws. *SIAM Review*, 25:35–61, 1983.

[18] P. Helluy, F. Golay, J.-P. Caltagirone, P. Lubin, S. Vincent, D. Drevard, R. Marcer, P. Fraunie, N. Seguin, S. Grilli, A.-C. Lesage, A. Dervieux, and O. Allain. Numerical simulations of wave breaking. *ESAIM: M2AN*, 39:591–607, 2005.

[19] W. D. Henshaw and D. W. Schwendeman. Moving overlapping grids with adaptive mesh refinement for high-speed reactive and non-reactive flow. *J. Comput. Phys.*, 216:744–779, 2006.

[20] K. A. Hoffmann and S. T. Chiang. *Computational Fluid Dynamics.* Engineering Education System, Wichita, Kansas, USA, 4 edition, 2000.

[21] W. H. Hui and S. Koudriakov. A unified coordinate system for solving the three-dimensional Euler equtions. *J. Comput. Phys.*, 172:235–260, 2001.

[22] W. Jang, J. Jilesen, F. S. Lien, and H. Ji. A study on the extension of a VOF/PLIC based method to curvilinear coordinate system. *Int. J. Comput. Fluid Dyn.*, 22(4):241–257, 2008.

[23] R. J. LeVeque. High resolution finite volume methods on arbitrary grids via wave propagation. *J. Comput. Phys.*, 78:36–63, 1988.

[24] R. J. LeVeque. *Numerical Methods for Conservation Laws.* Birkhäuser-Verlag, 2 edition, 1992.

[25] R. J. LeVeque. Wave propagation algorithms for multi-dimensional hyperbolic systems. *J. Comput. Phys.*, 131:327–353, 1997.

[26] R. J. LeVeque. *Finite Volume Methods for Hyperbolic Problems.* Cambridge University Press, 2002.

[27] R. J. LeVeque. *Finite Difference Methods for Ordinary and Partial Differential Equations: Steady-State and Time-Dependent Problems.* SIAM, Philadelphia, 2007.

[28] T. G. Liu, B. C. Khoo, K. S. Yeo, and C. Wang. Underwater shock-free surface-structure interaction. *Int. J. Numer. Meth. Engng*, 58:609–630, 2003.

[29] R. Menikoff and B. Plohr. The Riemann problem for fluid flow of real materials. *Rev. Mod. Phys.*, 61:75–130, 1989.

[30] G. Perigaud and R. Saurel. A compressible flow model with capillary effects. *J. Comput. Phys.*, 209:139–178, 2005.

[31] F. Petitpas, J. Massoni, R. Saurel, E. Lapebie, and L. Munier. Diffuse interface model for high speed cavitating underwater systems. *Int. J. Multiphase Flow*, 35:747–759, 2009.

[32] R. Saurel, F. Petitpas, and R. A. Berry. Simple and efficient relaxation methods for interfaces separating compressible fluids, cavitating flows and shocks in multiphase mixtures. *J. Comput. Phys.*, 228:1678–1712, 2009.

[33] C.-W. Shu. Essentially non-oscillatory and weighted essentially non-oscillatory schemes for hyperbolic conservation laws. In B. Cockburn, C. Johnson, C.-W. Shu, and E. Tadmor, editors, *Advanced Numerical Approximation of Nonlinear Hyperbolic Equations*, pages 325–432. Springer, Berlin, 1998. Lecture Notes in Mathematics, vol. 1697.

[34] K.-M. Shyue. An efficient shock-capturing algorithm for compressible multicomponent problems. *J. Comput. Phys.*, 142:208–242, 1998.

[35] K.-M. Shyue. A fluid-mixture type algorithm for compressible multicomponent flow with van der Waals equation of state. *J. Comput. Phys.*, 156:43–88, 1999.

[36] K.-M. Shyue. A fluid-mixture type algorithm for compressible multicomponent flow with Mie-Grueneisen equation of state. *J. Comput. Phys.*, 171:678–707, 2001.

[37] K.-M. Shyue. A fluid-mixture type algorithm for barotropic two-fluid flow problems. *J. Comput. Phys.*, 200:718–748, 2004.

[38] K.-M. Shyue. A volume-fraction based algorithm for hybrid barotropic and non-barotropic two-fluid flow problems. *Shock Waves*, 15(6):407–423, 2006.

[39] K.-M. Shyue. A moving-boundary tracking algorithm for inviscid compressible flow. In *Hyperbolic Problems: Theory, Numerics, Applications*, pages 989–996. Springer-Verlag, 2008.

[40] K.-M. Shyue. *Front Tracking Methods based on Wave Propagation*. Ph.D. thesis, University of Washington, June, 1993 (unpublished). Available at the URL http://www.math.ntu.edu.tw/∼shyue/preprints/thesis.pdf.

[41] G. Strang. On the construction and comparison of difference schemes. *SIAM J. Numer. Anal.*, 5:506–517, 1968.

[42] P. K. Sweby. High resolution schemes using flux limiters for hyperbolic conservation laws. *SIAM J. Numer Anal.*, 21:995–1011, 1984.

[43] M. Tanaka. The stability of solitary waves. *Phys. Fluids*, 29:650–655, 1986.

[44] J. F. Thompson, B. K. Soni, and N. P. Weatherill. *Handbook of Grid Generation*. CRC Press, 1999.

[45] E. F. Toro. *Riemann Solvers and Numerical Methods for Fluid Dynamics: A Practical Introduction, 2nd Edition*. Springer-Verlag, 1999.

[46] E. F. Toro, M. Spruce, and W. Speares. Restoration of the contact surface in the HLL-Riemann solver. *Shock Waves*, 4:25–34, 1994.

[47] P. Wesseling. *Principles of Computational Fluid Dynamics*. Springer-Verlag, 2001.

[48] P. Woodward and P. Colella. The piece-wise parabolic method (PPM) for gas dynamical simulations. *J. Comput. Phys.*, 54:174–201, 1984.

[49] H. W. Zheng, C. Shu, and Y. T. Chew. An objected-oriented quadrilateral-mesh based solution adaptive algorithm for compressible multifluid flows. *J. Comput. Phys.*, 227:6895–6921, 2008.

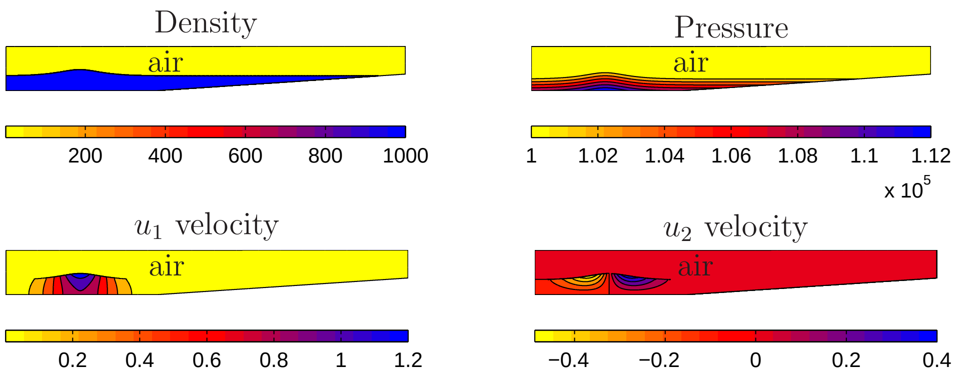

Figure 16: Filled contours of the initial states for a water wave breaking problem.

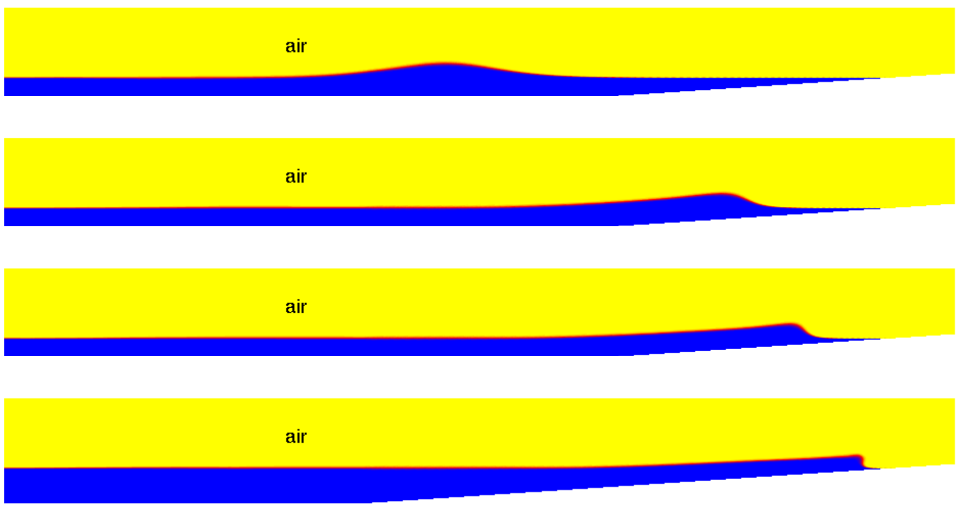

Figure 17: Pseudo-color images of the computed density for a water wave breaking problem with a 1800×200 grid. Results from top to bottom are at times $t = 2$, 4, 4.5, and 5s.

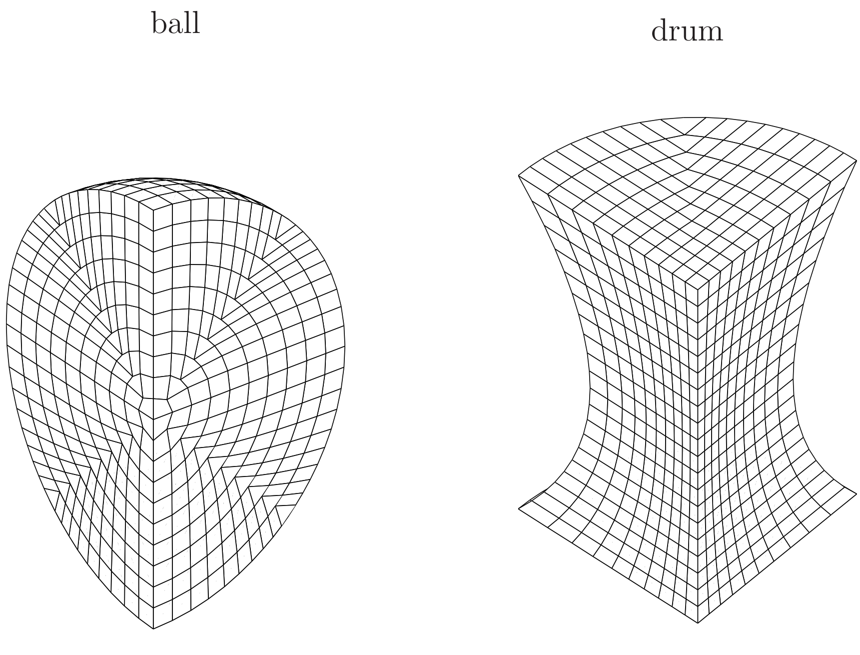

Figure 18: A cut-away views of a hexahedral grid in a three-dimensional domain. On the left, the domain is a ball, and on the right, the domain is a drum.

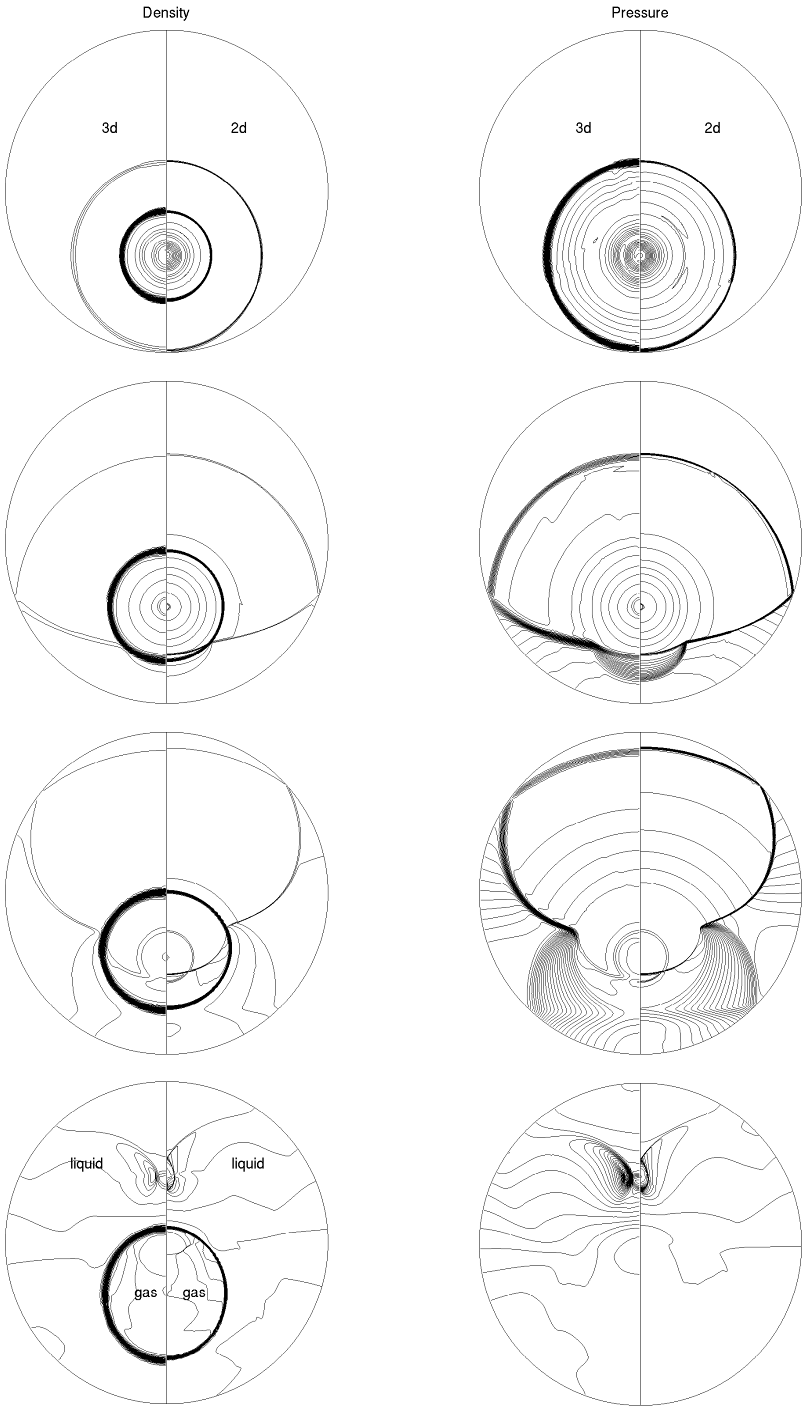

Figure 19: Contours the density and pressure for a blast wave problem in a unit ball. Solutions from the top to bottom are at times $t = 0.2$, 0.4, 0.6, and 1.0ms. At each plot, the three-dimensional result is on the left half, and the two-dimensional axisymmetric result is on the right half.

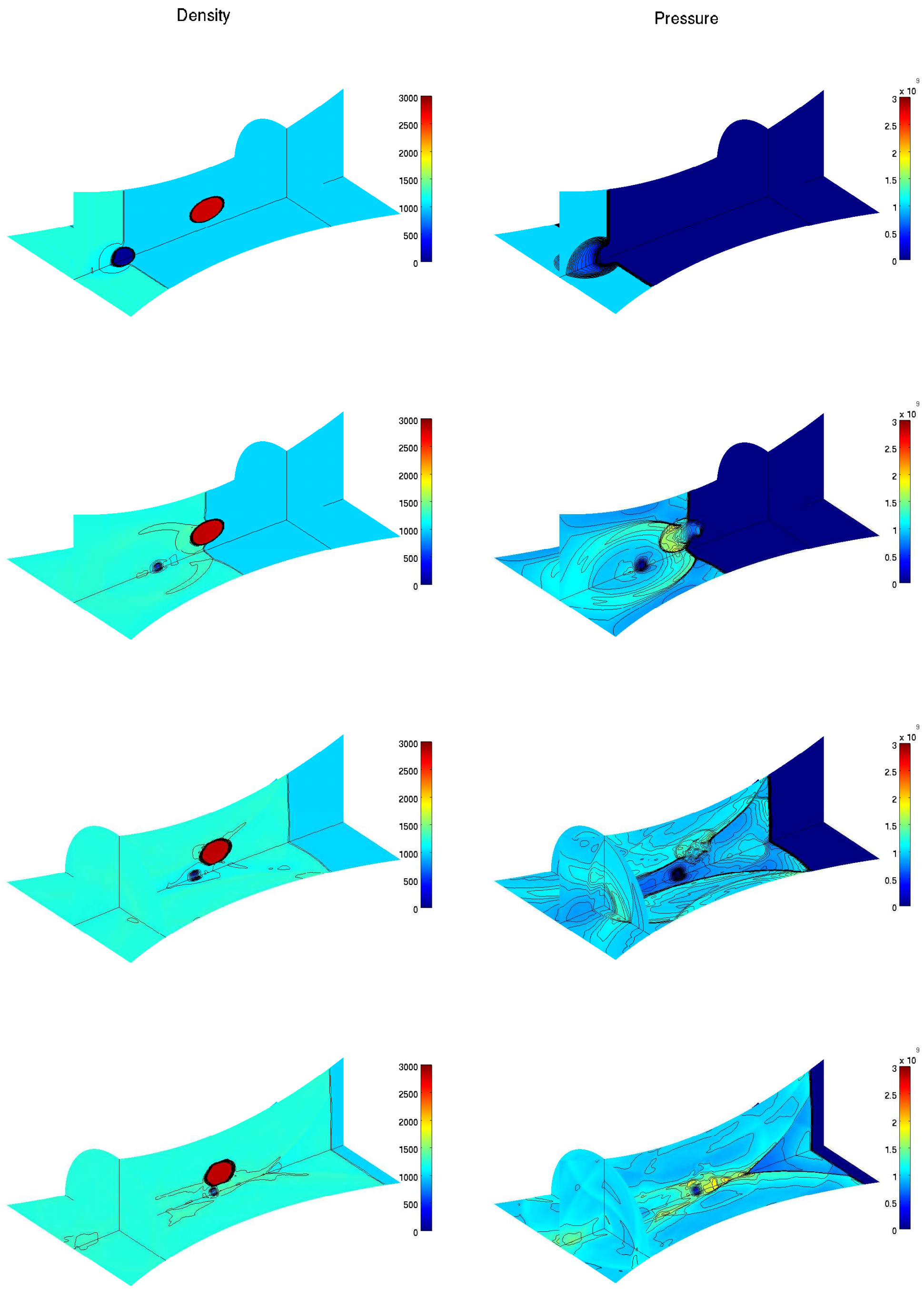

Figure 20: Pseudo-colors of the density and pressure for a shock wave over two spherical dispersed phases in a nozzle. Solutions from the top to bottom are at times $t = 0.2$, 0.6, 1.0, and 1.2ms, where at each plot there are three slice planes. We use a $240 \times 160 \times 80$ grid for the computation.